# Multiscale Analysis of Dynamics and Interactions of Heterochromatin Protein 1 by Fluorescence Fluctuation Microscopy

Katharina P. Müller,[†] Fabian Erdel,[†] Maïwen Caudron-Herger,[†] Caroline Marth,[†] Barna D. Fodor,[‡] Mario Richter,[‡] Manuela Scaranaro,[‡] Joël Beaudouin,[§¶] Malte Wachsmuth,[‖] and Karsten Rippe[†*]

[†]Deutsches Krebsforschungszentrum and BioQuant, Research Group Genome Organization and Function, Heidelberg, Germany; [‡]Research Institute of Molecular Pathology, Vienna, Austria; [§]Deutsches Krebsforschungszentrum and BioQuant, Research Group Intelligent Bioinformatics Systems, Heidelberg, Germany; [¶]Institute for Pharmacy and Molecular Biotechnology, University of Heidelberg, Heidelberg, Germany; and [‖]European Molecular Biology Laboratory, Cell Biology/Biophysics Unit, Heidelberg, Germany

ABSTRACT Heterochromatin protein 1 (HP1) is a central factor in establishing and maintaining the repressive heterochromatin state. To elucidate its mobility and interactions, we conducted a comprehensive analysis on different time and length scales by fluorescence fluctuation microscopy in mouse cell lines. The local mobility of HP1$\alpha$ and HP1$\beta$ was investigated in densely packed pericentric heterochromatin foci and compared with other bona fide euchromatin regions of the nucleus by fluorescence bleaching and correlation methods. A quantitative description of HP1$\alpha/\beta$ in terms of its concentration, diffusion coefficient, kinetic binding, and dissociation rate constants was derived. Three distinct classes of chromatin-binding sites with average residence times $t_{res} \leq 0.2$ s (class I, dominant in euchromatin), 7 s (class II, dominant in heterochromatin), and ~2 min (class III, only in heterochromatin) were identified. HP1 was present at low micromolar concentrations at heterochromatin foci, and required histone H3 lysine 9 methylases Suv39h1/2 for two- to fourfold enrichment at these sites. These findings impose a number of constraints for the mechanism by which HP1 is able to maintain a heterochromatin state.

## INTRODUCTION

The organization of the DNA genome in the nucleus by histones and other chromosomal proteins is controlled by epigenetic regulatory networks that modulate the accessibility of the DNA for transcription, DNA repair, and replication machineries. At the resolution of the light microscope, two different compaction states of chromatin can be distinguished: the denser and transcriptionally repressed heterochromatin, and the more open and biologically active euchromatin (1,2). These functional states are established via the highly dynamic recruitment of histones and other chromosomal proteins, as well as covalent modifications of histones and DNA. Heterochromatin is characterized by its high content of repetitive DNA elements and repressive epigenetic marks such as DNA methylation and di- or trimethylation of the histone H3 lysine residues 9 and 27 (H3K9me2/3 and H3K27me2/3) and the histone H4 lysine residue 20 (H4K20me2/3), as well as hypoacetylation of histones. Large regions of heterochromatin are located at and around the centromeres and at the telomeres. In mouse cells, clusters of pericentric heterochromatin can be easily identified on microscopic images due to their intense staining by 4′,6-diaminidino-2-phenylindole (DAPI). The corresponding loci are also referred to as chromocenters and comprise A/T-rich repetitive sequences around the centromere (3).

Heterochromatin formation is mediated by multiple pathways that trigger de novo DNA methylation, modification of histone tails, and alteration of nucleosome positions or integrity. A central factor in establishing and maintaining the heterochromatic state is heterochromatin protein 1 (HP1). HP1 is evolutionary highly conserved, and homologs have been found from yeast (*Schizosaccharomyces pombe*) to humans (4–6). The ability of HP1 to induce large-scale chromatin compaction has been demonstrated in a mammalian cell line (7). Three HP1 isoforms in mouse and humans are known: HP1$\alpha$, HP1$\beta$, and HP1$\gamma$. These isoforms are similar in terms of amino acid sequence and structural organization, but differ in their nuclear localization. The two dominant species, HP1$\alpha$ and HP1$\beta$, are primarily (but not exclusively) associated with heterochromatin and colocalize in mouse cells, whereas HP1$\gamma$ localizes to a larger extent to euchromatin as well (5,8,9). In euchromatin, the HP1-associated silencing occurs via the formation of small repressive chromatin domains, partly independently of the histone methyltransferase Suv39h1 but in association with the JmjC domain-containing histone H3K36 demethylase dKDM4A (4,10,11). HP1 contains an N-terminal chromo-domain (CD) and a C-terminal chromoshadow-domain (CSD) connected by a flexible linker region. The CD interacts specifically with H3 histone tails that carry the K9me2/3 modification (12,13). Numerous interaction partners of HP1 have been reported in the literature, including Suv39h1, the linker histone variant H1.4, the DNA methyltransferases Dnmt1 and Dnmt3, and noncoding RNAs (2,6). In addition, HP1 is also able to form homo- or heteromultimers of its different isoforms (14,15). In a current model, heterochromatin assembly is

*Submitted April 8, 2009, and accepted for publication August 27, 2009.*

*Correspondence: Karsten.Rippe@dkfz.de

Barna D. Fodor's and Mario Richter's present address is Max Planck Institute of Immunobiology, Dept. of Epigenetics, Freiburg, Germany.

Editor: Jonathan B. Chaires.



0006-3495/09/12/2876/10 $2.00

doi: 10.1016/j.bpj.2009.08.057

nucleated by the targeting of HP1 via its CD to H3K9me2/3, and at the same time it interacts with Suv39h1/2 via the CSD. This feedback loop of HP1 binding-mediated H3K9 methylation promotes HP1 binding to adjacent nucleosomes and would provide a mechanism for the maintenance of heterochromatin as well as heterochromatin spreading (1,2,16).

Noninvasive methods based on optical high-resolution microscopy are ideally suited to probe the mobility and interactions of nuclear proteins in living cells. A frequently used method is fluorescence recovery after photobleaching (FRAP), in which the fluorescence in a part of the cell is bleached and the redistribution back to the equilibrium state is recorded. The resulting recovery data contain information about the diffusion and binding processes of the labeled proteins. The initial FRAP studies of HP1 revealed that the protein is highly mobile in the nucleus and in frequent turnover between its chromatin-bound state and the freely mobile state in the nucleoplasm (17,18). In those experiments, halftimes of the FRAP recovery curves of 0.6–10 s for the freely mobile state and 2.5–50 s for the chromatin-bound state were determined. Further studies conducted with different cell types confirmed the high mobility of HP1 in euchromatin as well as in heterochromatin (8,19,20). Subsequently, more detailed FRAP analyses and kinetic modeling studies of HP1 concluded that the nuclear HP1 pool can be separated into at least three fractions: a highly mobile fraction; a less mobile, transiently binding fraction; and a smaller immobilized fraction (15,21). From FRAP studies of yeast, a model was derived that had differences in the kinetic on and off rates of HP1 binding to the unmethylated and the methylated nucleosome state (21).

Although these studies provided a wealth of information, the classical FRAP approach is limited in its spatial and temporal resolution, and information on local mobility on the subsecond timescale is not easily accessible. Here, we investigated the diffusion and interaction behavior of HP1$\alpha$ and HP1$\beta$ in living cells with a complementary set of fluorescence fluctuation microscopy approaches that included FRAP, continuous fluorescence photobleaching (CP), fluorescence loss in photobleaching (FLIP), and fluorescence correlation spectroscopy (FCS). Together, these techniques provide a comprehensive description of the spatially resolved mobility of the two proteins (22). From a quantitative analysis of the data according to a reaction-diffusion model, we derived a model for the interaction of HP1$\alpha/\beta$ with chromatin that dissects differences in its binding to heterochromatin and euchromatin. The increased binding affinity to heterochromatin was dependent on the presence of the Suv39h1/2 methylase. This demonstrates the existence of a direct linkage between an epigenetic modification and the interaction affinity of the corresponding readout protein in living mammalian cells.

## MATERIALS AND METHODS

Experiments were conducted with green fluorescent protein (GFP) constructs of mouse HP1$\alpha$ and HP1$\beta$, and a red fluorescent Suv39h1 fusion protein (TagRFP-Suv39h1) in the murine NIH 3T3 fibroblast cell line or in immortalized mouse embryonic fibroblasts (iMEF). For HP1$\alpha$ the cell line 3T3-HP1$\alpha$ was used, in which one allele of the HP1$\alpha$ gene was replaced by a GFP-HP1$\alpha$-coding sequence driven by a mouse PGK promoter. HP1$\beta$ was introduced via transient transfection. The contribution of the Suv39h1/2 methylases on HP1$\beta$ mobility was studied in an iMEF double null mutant (iMEF-dn) cell line that had the Suv39h1 and Suv39h2 genes disrupted, and lacked H3K9 di- and trimethylation in pericentric heterochromatin (23).

### Profile FRAP

For profile FRAP (pFRAP), the fluorescence intensity profile was determined for each picture of the time series perpendicular to a strip (3 $\mu$m wide) that was bleached through the nucleus to follow the broadening of the bleach profile due to diffusion (24). The data were analyzed with a confined diffusion model.

### Intensity-based FRAP experiments

The time evolution of the intensity integrated over the bleach spot was recorded (24), and the resulting data sets were analyzed according to the theoretical framework developed by McNally and co-workers (25). The data were fitted to a diffusion model, a binding model, or a reaction-diffusion model that incorporates both diffusion and binding processes.

### CP and FLIP

In the CP experiments, the decay of the fluorescence signal to the dynamic equilibrium of photobleaching, diffusion, and chromatin dissociation/association of GFP-HP1$\alpha$ was used to derive the kinetic dissociation rate (24,26). In the FLIP experiments, the fluorescence loss within heterochromatin and euchromatin regions was monitored between repetitive bleach pulses at distant regions from the bleach spot within the same nucleus (27).

### FCS

The FCS experiments were conducted as described previously (24). The data were fitted to a one- or two-component anomalous diffusion model, which is characterized by a nonlinear time dependency of the mean-squared particle displacement given by the anomaly parameter $\alpha$. Alternatively, a two-species model was applied in which the first component followed anomalous diffusion and the second component was assumed to be bound to a slowly and confinedly moving lattice.

A detailed description of all methods used and the data analyses of the FRAP, CP, FLIP, and FCS experiments is given in the Supporting Material.

## RESULTS AND DISCUSSION

HP1 is a central factor in establishing and maintaining a biologically inactive heterochromatin state (1,2). To describe the spatially resolved mobility and binding interactions of HP1$\alpha$ and HP1$\beta$, we applied a set of complementary fluorescence fluctuation microscopy methods (i.e., FRAP, CP, FLIP, and FCS). In the first pioneering FRAP studies of HP1, a fast transition between the free and chromatin-bound states of the protein was observed (17,18). Subsequent studies identified fractions of differently mobile molecules and calculated kinetic rates (8,15,19–21). The highly dynamic nature of the HP1-chromatin interaction raises the question as to how HP1 can mediate the formation of a stable heterochromatin state, and how its mode of interaction differs between euchromatin and heterochromatin. That issue was addressed in this

study. Since for HP1 the time to associate with a binding site is fast as compared to the time to diffuse across the bleach spot, both the binding kinetics and the diffusion must be accounted for in the quantitative description of the FRAP recovery curves (28). Accordingly, we took advantage of previous advancements in the analysis of FRAP data (25) to dissect the contribution of diffusion and binding interactions. Furthermore, FCS experiments with high spatial and temporal resolution were conducted to obtain additional data for the extraction of mobility and interaction parameters, as well as valuable information on the spatially resolved protein concentrations.

### HP1$\alpha$ and HP1$\beta$ are localized in heterochromatin foci at a 2–4 fold higher concentration than in euchromatin

GFP-HP1$\alpha$ and the TagRFP/GFP-HP1$\beta$ fusion protein were enriched in the pericentric heterochromatin foci (Fig. 1, *A–C*).

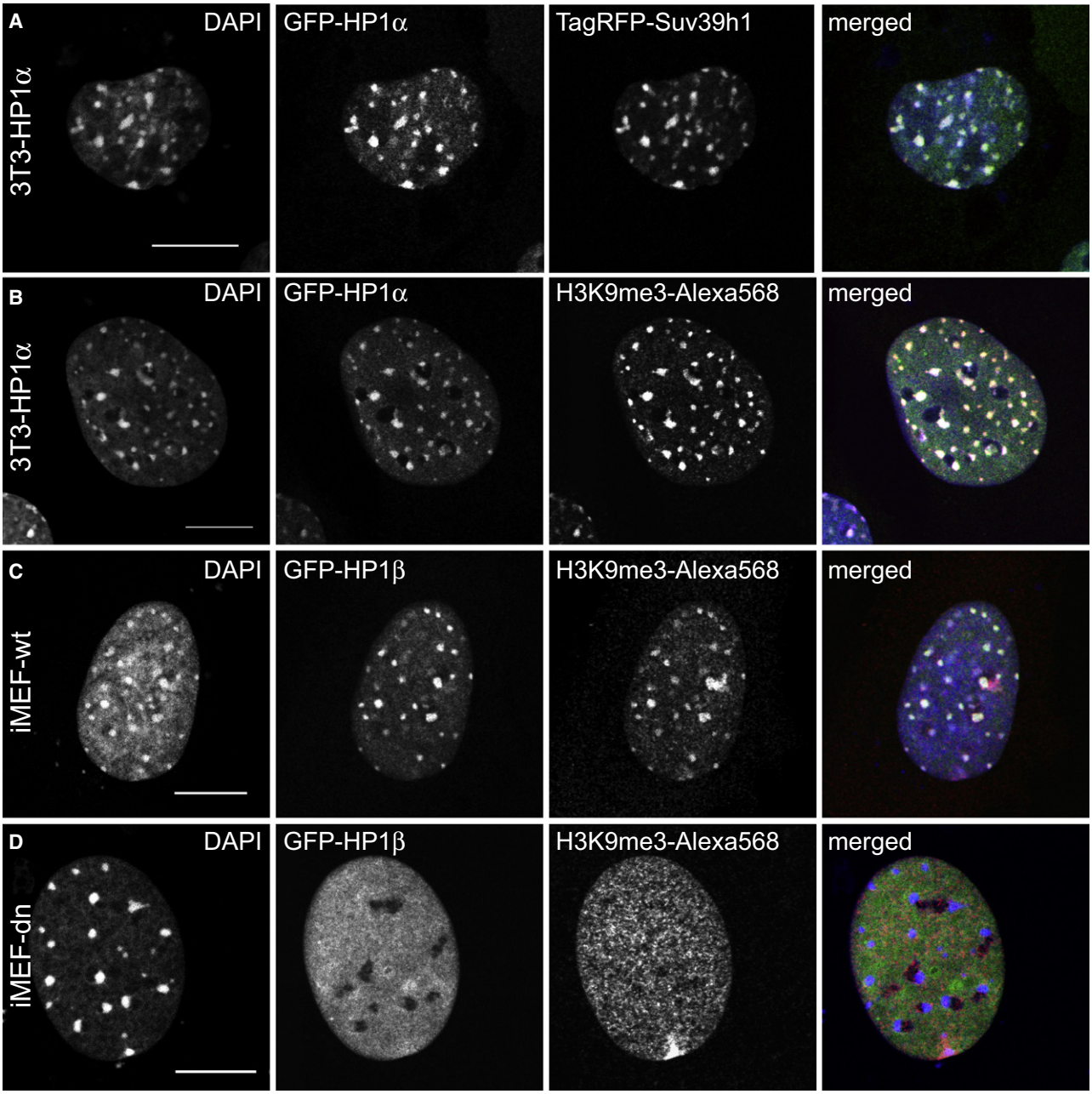


FIGURE 1 Localization of HP1 in the nucleus of 3T3 cells and iMEFs. HP1$\alpha$ was enriched in pericentric heterochromatin foci that are identified by increased DAPI staining. The scale bar is 10 $\mu$m. (*A*) Transfection of 3T3-HP1$\alpha$ cells with TagRFP-Suv39h1 reveals the colocalization of the two proteins. (*B*) Anti-H3K9me3 immunostaining shows that HP1$\alpha$ colocalizes with the H3K9me3 modification. (*C*) In iMEF-wt cells, GFP-HP1$\beta$ and the histone H3 lysine 9 trimethylation mark colocalize in pericentric heterochromatin, as in the 3T3-HP1$\alpha$ cell line. (*D*) The iMEF-dn double null mutant lacking the H3K9 histone methyltransferases Suv39h1 and Suv39h2 displays no trimethylation at the chromocenters, and the HP1$\beta$ distribution is diffuse.

Immunostaining against H3K9me3 yielded the expected colocalization with the HP1$\alpha$-enriched chromocenters (Fig. 1 *B*) and the Suv39h1 histone methyltransferase (Fig. 1 *A*). When we compared the iMEF wild-type cells (iMEF-wt) with the iMEF-dn mutant for Suv39h1/2 (Fig. 1, *C* and *D*), it was apparent that in the double null cells the H3K9me3 modification was absent and that HP1$\beta$ was distributed homogeneously in the nucleus and no longer targeted to the chromocenters (23). It should be noted that these persisted in the absence of HP1 binding and the H3K9me3 modification, which can be seen in the DAPI stain.

We evaluated the HP1 protein density and the DNA density (via DAPI staining) within euchromatin and heterochromatin regions in 3T3-HP1$\alpha$ cells by calculating the average fluorescence intensity within a defined region of interest. The DAPI staining showed a 2.0 $\pm$ 0.3-fold higher intensity in heterochromatin as compared to euchromatin. The enrichment of the GFP-HP1$\alpha$ signal in the heterochromatin foci was 2.0 $\pm$ 0.3-fold, and for GFP-HP1$\beta$ it was 4.4 $\pm$ 1.3-fold compared to euchromatin. Thus, only a moderate enrichment of HP1$\alpha$ and $\beta$ in heterochromatin as compared to euchromatin was apparent in this type of analysis.

## Spatial pFRAP analysis demonstrates a significant contribution of diffusion to the recovery curves

We investigated the contributions of diffusion and binding to the recovery kinetics of HP1$\alpha$ by bleaching a strip through the cell nucleus and evaluating the time evolution of the intensity profile (Fig. 2). For a purely binding-dominant recovery, the boundary of the bleached region would remain essentially unchanged and the reequilibration of the fluorescence intensity would proceed via an increase of the amplitude of the bleach profile (24). For HP1$\alpha$ and HP1$\beta$, the shape of the initially rectangular bleach profile broadened. Thus, diffusion made a significant contribution to the redistribution process, which was well described by a confined diffusion model according to the equations in the Supporting Material. The resulting diffusion coefficient $D_{\text{global}} = 1.4 \pm 0.3\ \mu\text{m}^2\ \text{s}^{-1}$ (Fig. 2, *B* and *C*, and Table 1) represents the averaged nuclear mobility of HP1$\alpha$. It includes the contribution of transient binding events that manifest themselves as a reduction of the apparent diffusion coefficient, whereas more long-lived interactions were insignificant during the relatively short data acquisition time of 5.6 s. This is apparent when we compare the value $D_{\text{global}} = 1.4 \pm 0.3\ \mu\text{m}^2\ \text{s}^{-1}$ with the expected mobility of free HP1 monomer and dimer with and without GFP label as calculated from all-atom model structures (Table S1). Including a correction to the ~3.5-fold higher effective viscosity within the cell, this yields values of 19.6 $\mu\text{m}^2\ \text{s}^{-1}$ and 17.5 $\mu\text{m}^2\ \text{s}^{-1}$ for HP1 dimers carrying one and two GFP tags, respectively, and 22.3 $\mu\text{m}^2\ \text{s}^{-1}$ for a GFP-HP1 monomer. Thus, for the evaluation of the HP1 FRAP recovery curves, both diffusion and binding make significant contributions and have to be taken into account explicitly, as previously concluded (29).

## FRAP experiments identify differences in HP1 binding to euchromatin and heterochromatin that depend on the Suv39h1/2 methylase

To identify differences in the diffusion kinetics and binding of HP1 in euchromatin and heterochromatin, we performed FRAP experiments. Spherical regions of the dimension of heterochromatin foci with an effective diameter of 1.9 $\mu$m were bleached in either heterochromatin or euchromatin (Fig. 3 *A* and Table 1). The redistribution of fluorescently labeled HP1 was recorded in sequential imaging scans and plotted versus time (Fig. 3 *B*). This intensity-based

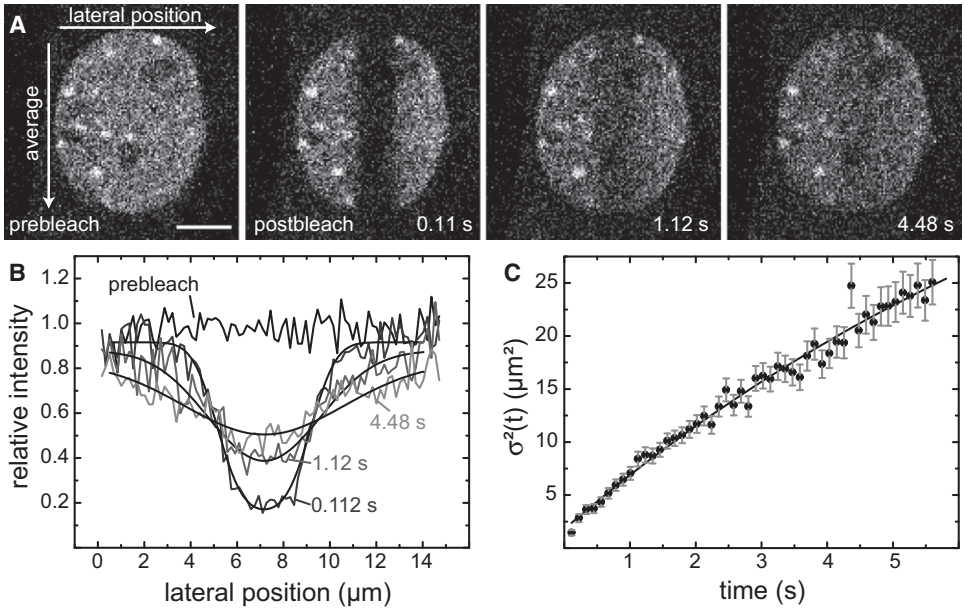


FIGURE 2 Boundary shape analysis in pFRAP. (*A*) Time series in which a rectangular region across the nucleus was bleached. Selected images of the time series are shown. Scale bar: 5 $\mu$m. For the analysis, the intensity was averaged in parallel to the bleach region and subsequently the corresponding profile perpendicular to it was plotted. (*B*) Intensity profiles for pre- and postbleach time points and the corresponding fit curves. (*C*) The profiles of 50 postbleach curves were analyzed with a confined diffusion model.

**TABLE 1 FRAP analysis of HP1$\alpha$ and HP1$\beta$**

| | 3T3-HP1$\alpha$ | | NIH 3T3 HP1$\beta$ | | iMEF-wt HP1$\beta$ | | iMEF-dn HP1$\beta$ * |
|---|---|---|---|---|---|---|---|
| | Euchromatin[†] | Heterochromatin[‡] | Euchromatin[†] | Heterochromatin[‡] | Euchromatin[†] | Heterochromatin[‡] | |
| $D_{app}$[†,‡] ($\mu m^2\ s^{-1}$) | 0.13 ± 0.03 | 0.9 ± 0.5 | 0.24 ± 0.06 | 1.5 ± 0.7 | 0.4 ± 0.1 | 2.3 ± 0.4 | 0.4 ± 0.1 |
| $k_{off}$[‡] ($s^{-1}$) | — | 0.15 ± 0.04 | — | 0.4 ± 0.1 | — | 0.6 ± 0.1 | — |
| $k^*_{on}$[‡] ($s^{-1}$) | — | 0.41 ± 0.12 | — | 2.0 ± 0.6 | — | 1.7 ± 0.1 | — |
| Free[‡] (%) | — | 24 ± 3 | — | 18 ± 8 | — | 25 ± 2 | — |
| Bound[‡] (%) | — | 65 ± 3 | — | 74 ± 8 | — | 75 ± 2 | — |
| $f_{im}$[†,‡] (%) | 1 ± 2 | 11 ± 4 | 2 ± 2 | 8 ± 5 | 2 ± 2 | 7 ± 3 | 1 ± 1 |
| $D_{global}$[§] ($\mu m^2 s^{-1}$) | 1.4 ± 0.3 | | 0.9 ± 0.1 | | n. d.[¶] | | n. d.[¶] |

Measurements were conducted with the stable 3T3-HP1$\alpha$ cell line, with GFP-HP1$\beta$ transiently transfected into NIH 3T3 cells, the wild-type mouse embryonic fibroblasts (iMEF-wt), or the iMEF-dn cells that are double null for the histone methylases Suv39h1 and Suv39h2. Errors correspond to a 95% confidence interval. See also the Supporting Material.

*In these cells, HP1 did not colocalize with the chromocenters, although they were still present as evident from the DAPI staining (Fig. 1 *D*). Measurements were conducted both in chromocenters as identified by a histone H2A-mRFP1 chromatin signal and in adjacent decondensed chromatin regions. The results were indistinguishable with respect to the values determined for $D_{app}$ and the immobile fraction, and were well described by a diffusion-only model as applied to euchromatin in the three other cell lines (see below). Accordingly, only the average value of measurements at both dense and open chromatin locations is given for the iMEF-dn cell line.

[†]GFP-HP1 mobility in euchromatin is well described by a diffusion-dominant model that has only $D_{app}$ and the immobile fraction $f_{im}$ as fit parameters. The value of the apparent diffusion coefficient $D_{app}$ also includes some contribution of transient binding to HP1 mobility.

[‡]In heterochromatin, a reaction-diffusion model was applied in the data analysis (see text). The values for the iMEF-wt cells were obtained by fitting the average of 24 FRAP measurements.

[§]Effective diffusion coefficient $D_{global}$ is an average over different chromatin domains and was obtained by pFRAP analysis, in which a strip through the nucleus is bleached.

[¶]Not determined.

evaluation of FRAP measurements demonstrated that HP1$\alpha$ in the 3T3-HP1$\alpha$ cell line was highly mobile within the nucleoplasm, especially in euchromatin domains, and somewhat less mobile in the heterochromatin foci. Whereas in euchromatin the recovery of bleached GFP-HP1$\alpha/\beta$ was complete in 60 s, in heterochromatin a 10% fraction was identified that was immobilized during this time period (Table 1).

To gain additional quantitative information about the distribution of diffusive or transiently binding fractions, we applied three different models to the analysis of the FRAP data: 1), the diffusion-dominant model (Fig. S1, *A* and *D*) assuming that proteins are freely mobile; 2), the reaction-dominant model (Fig. S1, *B* and *E*), in which diffusion is assumed to be very fast compared to binding on the timescale of the FRAP measurement; and 3), the diffusion-reaction model, which considers contributions from both binding and diffusion on similar timescales (Fig. S1, *C* and *F*). The quality of the fit to the three different models was evaluated by a statistical *F*-test (Supporting Material). In euchromatin (Fig. S1, *A–C*) the best model was the diffusion-dominant model, and for HP1$\alpha$ in euchromatin $D_{app} = 0.13 \pm 0.03\ \mu m^2\ s^{-1}$ was obtained. The low value of the apparent diffusion coefficient $D_{app}$ reflects the contribution of transient binding events. Under the condition that $k^*_{on}\ \tau_D >> 1$, the binding contribution cannot be dissected from the diffusion term. In this case, the recovery curve can be described by a diffusion-dominant model with a reduced diffusion coefficient $D_{app} = D/(1 + k^*_{on}/k_{off})$. A lower boundary value of $k_{off} = 6.2\ s^{-1}$ was determined by comparing the fit quality of simulated recovery curves for different $k_{off}$ values (Supporting Material).

For the more complex dynamics of GFP-HP1$\alpha$ in heterochromatin, the diffusion-reaction model resulted in a significantly better fit (Fig. S1, *D–F*). The diffusion coefficient was determined to be $D_{app} = 0.9 \pm 0.5\ \mu m^2\ s^{-1}$ for the fraction of mobile molecules (~24% ± 3%). The interacting fraction comprised 65% ± 3% and had a dissociation constant of $k_{off} = 0.15 \pm 0.04\ s^{-1}$ corresponding to an average residence time of $t_{res} = 7$ s in the chromatin-bound state ($t_{res} = 1/k_{off}$; Table 1). For the 11% ± 4% fraction of immobilized HP1$\alpha$ molecules, the $t_{res}$ ~2 min was estimated from FRAP experiments in which the recovery was monitored over 5 min.

Measurements of HP1$\beta$ mobility in euchromatin and heterochromatin of iMEF-wt cells yielded results very similar to those obtained with the NIH 3T3 cells (Table 1). In particular, for heterochromatin, a fraction that was immobile on the minute scale was detected and a reaction-diffusion model was required to describe the data with $D_{app} = 2.3 \pm 0.4\ \mu m^2\ s^{-1}$ and $k_{off} = 0.6 \pm 0.1\ s^{-1}$ as compared to $D_{app} = 1.5 \pm 0.7\ \mu m^2\ s^{-1}$ and $k_{off} = 0.4 \pm 0.1\ s^{-1}$ in NIH 3T3 cells. In contrast, HP1$\beta$ mobility and chromatin interactions were very different in the iMEF-dn cell line that lacks Suv39h1/2 and H3K9 trimethylation in pericentric heterochromatin, and exhibits a homogeneous distribution of HP1$\beta$ in the nucleus (Fig. 1 *D*). Measurements were conducted in both open and dense chromatin regions as identified by a histone H2A-mRFP1 chromatin signal. Within both nuclear subcompartments, HP1$\beta$ mobility was indistinguishable in the FRAP experiments and almost identical to that observed in the euchromatic regions of NIH 3T3 and iMEF-wt cells. The mobility was well described by a diffusion model with $D_{app} = 0.4 \pm 0.1\ \mu m^2\ s^{-1}$ and a negligible immobile fraction

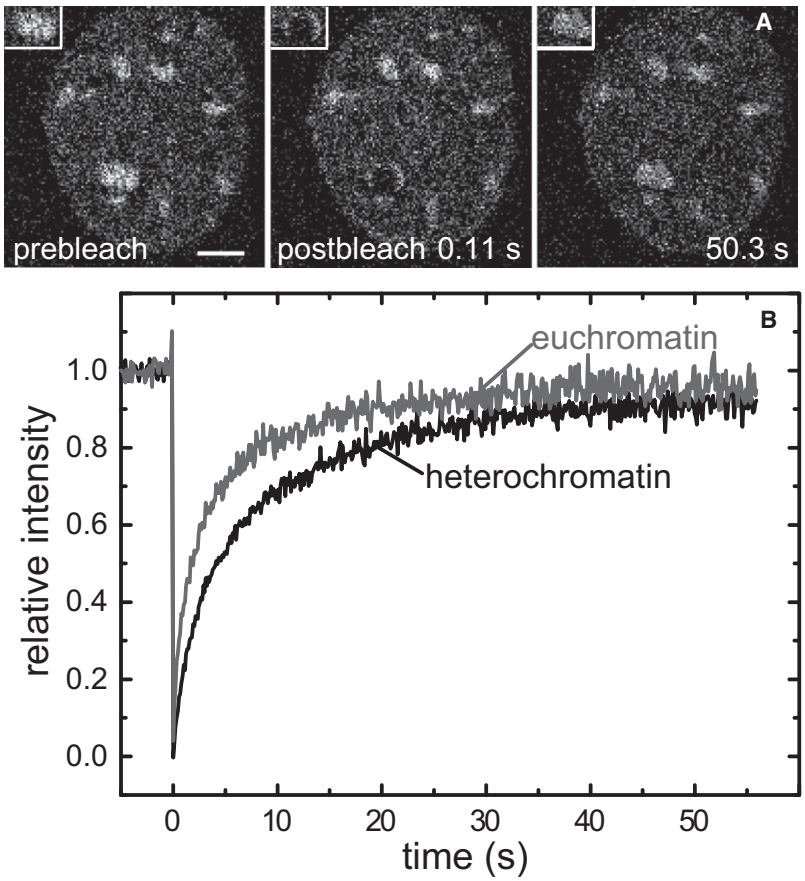


FIGURE 3 Diffusion and interaction analysis of HP1$\alpha$ in euchromatin and heterochromatin in 3T3-HP1$\alpha$ cells. (*A*) A circular region of interest with an effective diameter of 1.9 $\mu$m was bleached, and selected images of a time series are shown. The measurement was done within a heterochromatin focus and the insets show a zoomed image of the bleached area. The scale bar is 5 $\mu$m. (*B*) A comparison of the quantitative FRAP analysis in euchromatin and heterochromatin reveals a higher mobility in euchromatin. The curves represent average values from at least 10 cells.

(Table 1). This is likely the result of both the absence of the methylases themselves and the corresponding lack of the H3K9me3 modification in pericentric heterochromatin. It was previously shown that the H3K9me2/3 modification increases the binding affinity of the HP1 chromodomain to a H3 tail peptide with a $K_d$ of 2.5–4 $\mu$M (12,13). In addition, since HP1 and Suv39 proteins interact with each other, the binding of the two proteins to chromatin could be cooperative (16,30,31). This is in agreement with previous studies in yeast that reported an increase in the mobility of the HP1 family protein Swi6 in a strain deficient of the Clr4 histone methyltransferase, which has structural and functional similarities to the mammalian Suv39h1/2 proteins (21). Furthermore, it was shown that the ability of Clr4 to bind to the H3K9me3 mark via its chromodomain is important for maintaining heterochromatin, in addition to its catalytic histone methylation activity (32). Thus, it is concluded that the stronger-affinity binding sites for HP1 in heterochromatin are characterized by both the presence of the H3K9me2/3 modification and the enrichment of Suv39h1/2 protein bound at these sites.

### CP and FLIP experiments confirm the FRAP results obtained for HP1$\alpha$ binding to heterochromatin

The point CP experiments allow for the analysis of slow binding processes with better spatial resolution as compared to FRAP. From the temporal behavior of the mostly biphasic CP curves, the bound fraction and/or the dissociation rate or residence time at binding sites can be derived. The fraction of immobilized HP1 protein determined from FRAP experiments was included as a fixed parameter to obtain a robust fit value for the dissociation constant $k_{off}$ that was determined from the slower-decaying part of the curve (Fig. S2 *A*). The dissociation rate $k_{off} = 0.12 \pm 0.04\ s^{-1}$ was measured, which confirmed the results of the FRAP experiments with $k_{off} = 0.15 \pm 0.04\ s^{-1}$. In euchromatin, HP1$\alpha$ displayed fast interactions with $k_{off}/\alpha >> 1$. In this case, the measurement could not be decomposed into the bound and free ligand fractions, and therefore no off-rate could be determined (26). Measurements in the cytoplasm showed only a slow asymptotic decay (data not shown). This supports the conclusion that HP1 is a freely mobile species in this compartment.

The CP analysis was complemented with FLIP studies to observe the dissociation of the more tightly bound HP1$\alpha$ fraction. These experiments clearly revealed the differences between HP1$\alpha$ binding in heterochromatin and euchromatin in the 3T3-HP1$\alpha$ cell line (Fig. S2 *B*). After 10–20 s the differences in the protein dissociation processes were clearly visible in the bleaching curves. A maximum intensity difference of 8% $\pm$ 2% was observed at 70 $\pm$ 20 s. At this time point, a significant fraction of the interacting HP1 molecules

began to be replaced by bleached molecules. With FRAP, we measured an 11% HP1$\alpha$ fraction immobilized for at least 60 s in heterochromatin, which can be assigned to the stably bound HP1$\alpha$ fraction detected in the FLIP experiments.

### FCS measurements of HP1 provide spatially resolved effective diffusion coefficients, anomalous diffusion parameters, and concentrations

To further dissect GFP-HP1 mobility and interactions with better spatial and temporal resolution, we applied an FCS analysis. Expressions for an anomalous diffusion model with one or two components were found to best fit the autocorrelation function (ACF). In the cytoplasm, HP1 mobility was described by an anomalous diffusion model for a single, monodisperse species (Fig. 4, and Fig. S3 *A*). A mean diffusion time of $\tau_{diff} = 315 \pm 33$ $\mu$s and an anomaly parameter of $\alpha = 0.8 \pm 0.1$ were determined corresponding to

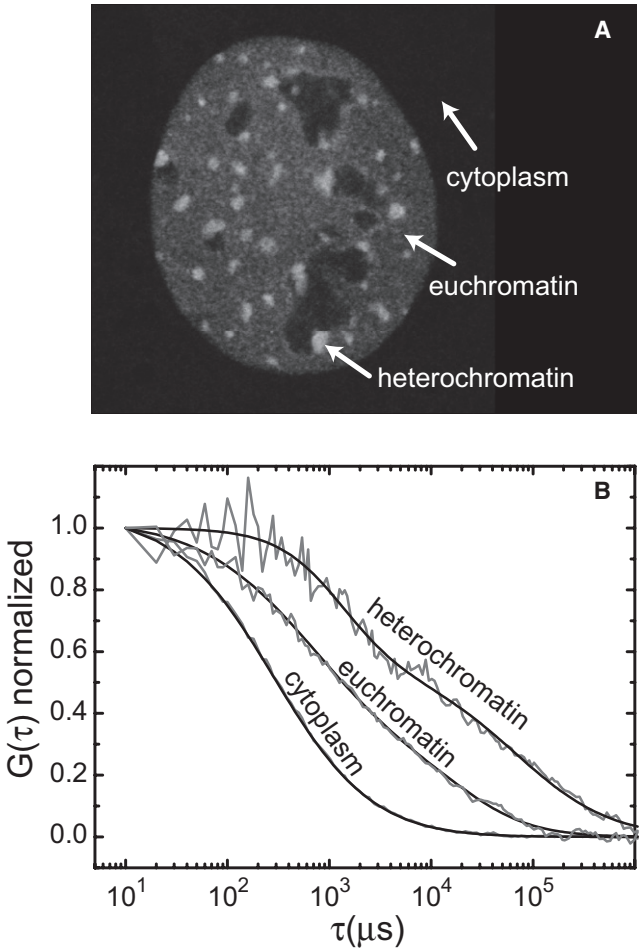


FIGURE 4 HP1$\alpha$ dynamics measured by FCS. (*A*) FCS experiments were conducted with 3T3-HP1$\alpha$ cells in the indicated cellular regions. (*B*) The normalized ACFs were fitted to an anomalous diffusion model (*solid line*). A one-component fit of data measured in the cytoplasm, and two-component fits of the euchromatin and heterochromatin data are displayed.

$D = 23 \pm 2$ $\mu m^2 s^{-1}$ (Table 2). This is similar to a previously reported measurement of $D = 26 \pm 2$ $\mu m^2 s^{-1}$ (15) and fits very well with the value predicted for a GFP-HP1 monomer of $D_{25°C,cell} = 22.3$ $\mu m^2 s^{-1}$ from hydrodynamic calculations when accounting for a 3.5-fold viscosity increase in the cytoplasm as compared to water (22) (Table S1). For a GFP-tagged HP1 dimer, somewhat lower values of 17–19 $\mu m^2 s^{-1}$ are expected (Table S1). FCS measurements of free GFP as a reference in the cytoplasm yielded $D = 24 \pm 5$ $\mu m^2 s^{-1}$. Thus, the comparison of the measured and calculated diffusion coefficients of GFP-HP1$\alpha$ and GFP alone indicate that GFP-HP1$\alpha$ is monomeric in the cytoplasm.

The ACFs obtained in euchromatin and heterochromatin required a two-component anomalous diffusion model, from which the diffusion coefficients of a highly mobile fraction and a second slow mobility fraction were extracted (Fig. 4, and Fig. S3, *C* and *D*). In euchromatin, the first component comprised 77% $\pm$ 3% with $\tau_{1,diff} = 973 \pm 95$ $\mu$s, $D_1 = 7.7 \pm 0.8$ $\mu m^2 s^{-1}$ and $\alpha_1 = 0.81 \pm 0.04$. The second fraction moved significantly more slowly with a diffusion time of $45 \pm 16$ ms and $\alpha > 1$, corresponding to $D_2 = 0.21 \pm 0.04$ $\mu m^2 s^{-1}$. The corresponding analysis in heterochromatin revealed a considerably smaller fast-moving fraction (~55% $\pm$ 4%) with a diffusion time of $\tau_{1,diff} = 2.1 \pm 0.6$ ms, $D_1 = 3.9 \pm 0.9$ $\mu m^2 s^{-1}$ and $\alpha_1 = 0.9 \pm 0.1$. Again the second species was much slower, with $\tau_{2,diff} = 223 \pm 69$ ms ($D_2 = 0.05 \pm 0.02$ $\mu m^2 s^{-1}$) and $\alpha > 1$. An anomaly parameter between one (free diffusion) and two (ballistic movement) can arise from energy-driven directed motion. For the determination of the anomaly parameter from FCS measurements, a value of $\alpha > 1$ can also originate from confined diffusion (26). Therefore, a second model was used in which all values for the first diffusive species were fixed to the values obtained from the first fit and the second species was modeled with a spatially confined mobility (Fig. S3, *C* and *D*, *dashed curves*). This approach resulted in a fit of equally good quality and diffusion coefficients of $0.20 \pm 0.05$ $\mu m^2 s^{-1}$ (euchromatin) and $0.04 \pm 0.01$ $\mu m^2 s^{-1}$ (heterochromatin) for the second species, which can be rationalized as the confined mobility of a chromatin fiber with bound HP1.

The inverse proportionality between the ACF amplitude and the protein concentration in FCS experiments was exploited to measure the concentration of GFP-HP1$\alpha$ in the cytoplasm, euchromatin, and heterochromatin, yielding values of $c_{cyt} = 0.16 \pm 0.11$ $\mu$M, $c_{eu} = 0.87 \pm 0.07$ $\mu$M, and $c_{het} = 2.1 \pm 0.3$ $\mu$M, respectively (Table S2). To compare the amount of fluorescently tagged GFP-HP1$\alpha$ and endogenously produced HP1$\alpha$, a quantitative Western blotting analysis was performed (Fig. S3 *B*). The amount of GFP-HP1$\alpha$ was measured to be 4.2 $\pm$ 0.5-fold higher than that of the endogenous protein. This corresponds to a concentration of endogenous HP1$\alpha$ monomer in the original untransfected 3T3 cell line of $c_{cyt} = 0.08 \pm 0.05$ $\mu$M, $c_{eu} = 0.41 \pm 0.05$ $\mu$M, and $c_{het} = 1.0 \pm 0.2$ $\mu$M. This is significantly lower than a previous estimate that reported one HP1 molecule per 15 nucleosomes

**TABLE 2 FCS measurements of HP1$\alpha$ and HP1$\beta$ in NIH 3T3 cells**

| | Cytoplasm* | | Euchromatin† | | Heterochromatin† | |
|---|---|---|---|---|---|---|
| | HP1$\alpha$ | HP1$\beta$ | HP1$\alpha$ | HP1$\beta$ | HP1$\alpha$ | HP1$\beta$ |
| $D_1$ ($\mu m^2\ s^{-1}$) | 23.4 ± 2.4 | 24.3 ± 5.6 | 7.7 ± 0.8 | 3.2 ± 0.8 | 3.9 ± 0.9 | 3.7 ± 0.6 |
| $\alpha_1$ | 0.83 ± 0.05 | 0.74 ± 0.05 | 0.81 ± 0.04 | 0.79 ± 0.06 | 0.88 ± 0.12 | 0.83 ± 0.08 |
| $D_2$ ($\mu m^2\ s^{-1}$) | — | — | 0.21 ± 0.04 | 0.07 ± 0.02 | 0.05 ± 0.02 | 0.04 ± 0.01 |
| $\alpha_2$ | — | — | >1 | >1 | >1 | >1 |

Data were analyzed with a one- or two-component anomalous diffusion model. As a reference, the diffusion constant of GFP was measured to be $D = 23.7 \pm 4.5\ \mu m^2\ s^{-1}$ in the cytoplasm ($\alpha = 0.97 \pm 0.04$) and $D = 21.5 \pm 4.8\ \mu m^2\ s^{-1}$ in the nucleus ($\alpha = 1.1 \pm 0.1$). Euchromatin and heterochromatin regions were not distinguishable in terms of the associated GFP mobility. See also the Supporting Material.

*The data for the HP1$\alpha$ and HP1$\beta$ mobility in the cytoplasm were fit with a one-component anomalous diffusion model ($D_1$, $\alpha_1$). (Error limits correspond to a 95% confidence interval.)

†For the nuclear fraction of HP1$\alpha$ and HP1$\beta$, a two-component model was required to describe the data. The faster-moving fraction with diffusion constant $D_1$ displayed a subdiffusion behavior ($\alpha < 1$), as expected for transient binding and/or diffusion in the presence of obstacles. For the second fraction, intensity fluctuations were very slow and displayed a value of $\alpha > 1$. A more detailed analysis of the associated intensity fluctuations revealed that they originate from chromatin-bound molecules and can be described by a confined diffusion model.

in a third instar larval nucleus in *Drosophila*, which would correspond to a total HP1 concentration of ~10 $\mu$M (5,33,34). Nevertheless, the micromolar concentration of HP1$\alpha$ could be sufficient to induce the formation of HP1 dimers via its chromoshadow domain, as inferred from in vitro experiments (S. Kaltofen and K. Rippe, unpublished results). In addition, it is conceivable that crowding effects, especially in the high-density heterochromatin areas, as well as binding of HP1 to chromatin could promote dimerization of the protein.

## Bleaching and correlation data can be integrated into a multiscale analysis of HP1 mobility and interactions

From the analysis of HP1$\alpha$ and HP1$\beta$ mobility at different time and length scales, a comprehensive mobility picture of HP1$\alpha/\beta$ in the nucleus was obtained. In heterochromatin, FRAP experiments revealed a specifically binding HP1 fraction with a dissociation rate $k_{off} = 0.15\ s^{-1}$, a value that was confirmed by CP experiments. This fraction was less abundant in euchromatin, which suggests that it arises from interactions with binding sites enriched in heterochromatin (referred to as class II sites). The diffusion coefficient for the mobile HP1 fraction in heterochromatin of $D_{app} = 0.9 \pm 0.5\ \mu m^2\ s^{-1}$ was in good agreement with the average value determined by pFRAP analysis ($D_{global} = 1.4 \pm 0.3\ \mu m^2\ s^{-1}$). The $D_{app}$ value reflects the free diffusion together with transient binding interactions that are too fast to be resolved (referred to here as class I sites). These are present in both euchromatin and heterochromatin. Using the FRAP data obtained in euchromatin, an upper boundary for the class I residence time of 0.2 s was obtained. From the FCS experiments, an effective diffusion coefficient of $D_{app} = 3.9 \pm 0.9\ \mu m^2\ s^{-1}$ for HP1 mobility that includes binding to the class I sites was determined in heterochromatin. This value is equivalent to the FRAP value if the scale dependence of the diffusion coefficient in the case of anomalous diffusion is taken into consideration (see the Supporting Material). Class II binding cannot be detected by FCS because the corresponding dissociation rate is larger than the typical bleaching rate (HP1 is bound for $1/k_{off} = 7$ s, whereas bleaching is complete within 1–2 s).

In euchromatin, FRAP experiments yielded an apparent diffusion coefficient of $D_{app} = 0.13 \pm 0.03\ \mu m^2\ s^{-1}$, which represents the HP1 mobility and interactions with binding sites of class I and class II. Class II binding sites cannot be resolved separately, which suggests that their contribution is less significant than in heterochromatin. When the FRAP data measured in euchromatin were fitted with a diffusion-reaction model using $k_{off} = 0.15\ s^{-1}$ of class II binding as a fixed parameter, a very low local concentration of class II binding sites was obtained, confirming this conclusion. FCS experiments in euchromatin yielded an apparent diffusion coefficient of $7.7 \pm 0.8\ \mu m^2\ s^{-1}$, which presumably includes the interaction between HP1 and class I binding sites. It is larger in euchromatin since the chromatin concentration (and thus the concentration of class I binding sites) is smaller than in heterochromatin, resulting in less HP1 binding and higher HP1 mobility. In addition, a 10% fraction of HP1$\alpha/\beta$ was detected in heterochromatin that had an average residence time of 2 min in the FRAP experiments. The corresponding higher-affinity binding sites are referred to here as class III binding sites.

In heterochromatin, the contribution of class II binding sites can be separated to calculate the pseudo-equilibrium constant $K^*_{eq} = k^*_{on}/k_{off} = k_{on}\ [S]_{eq}/k_{off}$, which includes the free binding site concentration $[S]_{eq}$, to be $K^*_{eq,II} = 2.7$ (see the Supporting Material). The pseudo-affinity for the class I binding sites can be determined based on the comparison of the free and apparent diffusion coefficients that incorporates transient binding interactions. The free diffusion coefficient was measured by FCS in the cytoplasm and scaled appropriately to yield a value of $K^*_{eq,I} = 15$, under the assumption that the decrease in the apparent diffusion coefficient is exclusively caused by binding interactions.

In euchromatin, binding to class I and class II cannot be separated, resulting in an apparent diffusion coefficient that contains both contributions. From the pseudo-binding

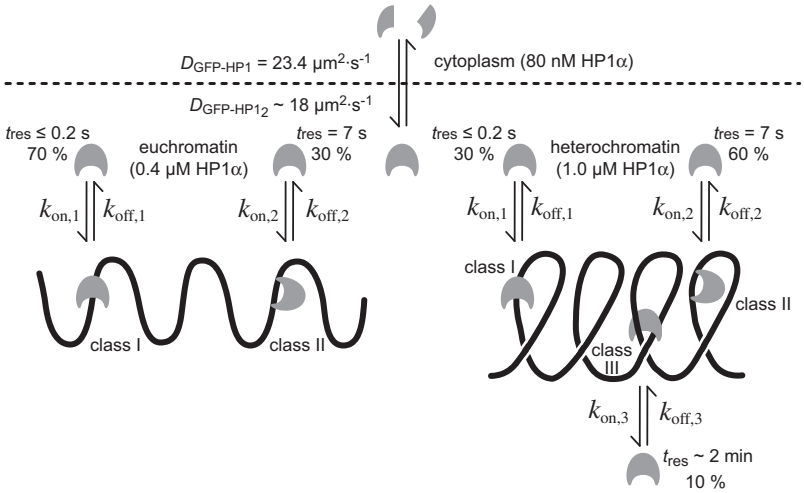


FIGURE 5 Kinetic model of HP1 mobility and interactions in the cell. A highly diffusive, noninteracting species was found in the cytoplasm. Different fractions of HP1 molecules were detected within the nucleus. A highly mobile fraction diffuses throughout the whole nucleus, showing unspecific binding interactions (class I); some HP1 molecules bind transiently but specifically to euchromatin or heterochromatin (class II); and a third fraction is stably incorporated into chromatin, probably via interaction with various binding partners (class III). Values for diffusion coefficients and residence times are given for HP1$\alpha$.

constants determined in heterochromatin, and the effective diffusion coefficient in euchromatin, relative fractions of 66% (class I) and 34% (class II) binding sites in euchromatin are estimated. To convert pseudo-binding constants into true binding affinities, the appropriate values of $[S]_{eq}$ must be known. To a first approximation, one can assume that the most abundant interaction partner of HP1 represented by the class I binding sites is a nucleosome. Accordingly, $[S]_{eq}$ can be related to the average nucleosome concentration of 140 $\mu$M (22). This would correspond to an affinity of $K_{eq,I} = 1.1 \pm 0.2\ 10^5\ M^{-1}$ for class I binding sites.

## CONCLUSIONS

The data obtained here can be reconciled in the model depicted in Fig. 5. In the cytoplasm, highly mobile monomeric HP1 was present. In the nucleus, three different binding sites can be identified: 1), one binding site that is ubiquitously present in chromatin (class I, $t_{res} \leq 0.2$ s); 2), one stronger binding site that is enriched in heterochromatin (class II, $t_{res} = 7$ s); and 3), the strongest binding site, which is present only in heterochromatin (class III, $t_{res} = 2$ min). It is also noteworthy that the ratio of class I to class II binding sites is ~2:1 in euchromatin and 1:2 in heterochromatin. Thus, the 2–4-fold enrichment of HP1$\alpha/\beta$ in heterochromatin originates from the twofold higher fraction of class II and the additional class III binding sites. As discussed above, these are likely to reflect an increase of the H3K9me2/3 modifications and/or the presence of Suv39h1/2 as an HP1-interacting protein (12,13,16,30,31). The concentration of HP1$\alpha/\beta$ in heterochromatin is in the low micromolar range and thus represents only a very small fraction of transiently associated protein as compared to the 200–300 $\mu$M nucleosome concentration (22). This imposes a number of constraints for the mechanism by which HP1, the Suv39h1/2 methylases, and the H3K9me2/3 modification cooperate to maintain a stable heterochromatin state that can cover several megabasepairs of DNA.

## SUPPORTING MATERIAL

Methods, equations, figures, tables, and references are available at http://www.biophysj.org/biophysj/supplemental/S0006-3495(09)01467-2.

We thank Thomas Höfer, Roland Eils, and Thomas Jenuwein for help and discussions. Parts of the fluorescence microscopy work were conducted at the Nikon Imaging Center at the University of Heidelberg, the Microscopy Core Facility of the German Cancer Research Center, and the Advanced Light Microscopy Facility of the European Molecular Biology Laboratory. We thank Natasha Murzina and Ken Yamamoto for the plasmid vectors, and Nick Kepper for help with calculating diffusion coefficients from model structures.

This project was supported by the German CellNetworks Cluster of Excellence (EXC81) and the SBCancer program within the Helmholtz Alliance on Systems Biology.

## REFERENCES

1. Grewal, S. I., and S. Jia. 2007. Heterochromatin revisited. *Nat. Rev. Genet.* 8:35–46.
2. Eissenberg, J. C., and G. Reuter. 2009. Cellular mechanism for targeting heterochromatin formation in *Drosophila*. *Int. Rev. Cell. Mol. Biol.* 273:1–47.
3. Probst, A. V., and G. Almouzni. 2008. Pericentric heterochromatin: dynamic organization during early development in mammals. *Differentiation.* 76:15–23.
4. Hiragami, K., and R. Festenstein. 2005. Heterochromatin protein 1: a pervasive controlling influence. *Cell. Mol. Life Sci.* 62:2711–2726.
5. Maison, C., and G. Almouzni. 2004. HP1 and the dynamics of heterochromatin maintenance. *Nat. Rev. Mol. Cell Biol.* 5:296–304.
6. Kwon, S. H., and J. L. Workman. 2008. The heterochromatin protein 1 (HP1) family: put away a bias toward HP1. *Mol. Cells.* 26: 217–227.
7. Verschure, P. J., I. van der Kraan, W. de Leeuw, J. van der Vlag, A. E. Carpenter, et al. 2005. In vivo HP1 targeting causes large-scale chromatin condensation and enhanced histone lysine methylation. *Mol. Cell. Biol.* 25:4552–4564.
8. Dialynas, G. K., S. Terjung, J. P. Brown, R. L. Aucott, B. Baron-Luhr, et al. 2007. Plasticity of HP1 proteins in mammalian cells. *J. Cell Sci.* 120:3415–3424.
9. Minc, E., Y. Allory, H. J. Worman, J. C. Courvalin, and B. Buendia. 1999. Localization and phosphorylation of HP1 proteins during the cell cycle in mammalian cells. *Chromosoma.* 108:220–234.

10. Hediger, F., and S. M. Gasser. 2006. Heterochromatin protein 1: don't judge the book by its cover! *Curr. Opin. Genet. Dev.* 16:143–150.

11. Lin, C. H., B. Li, S. Swanson, Y. Zhang, L. Florens, et al. 2008. Heterochromatin protein 1a stimulates histone H3 lysine 36 demethylation by the *Drosophila* KDM4A demethylase. *Mol. Cell.* 32:696–706.

12. Jacobs, S. A., and S. Khorasanizadeh. 2002. Structure of HP1 chromodomain bound to a lysine 9-methylated histone H3 tail. *Science.* 295: 2080–2083.

13. Fischle, W., Y. Wang, S. A. Jacobs, Y. Kim, C. D. Allis, et al. 2003. Molecular basis for the discrimination of repressive methyl-lysine marks in histone H3 by Polycomb and HP1 chromodomains. *Genes Dev.* 17:1870–1881.

14. Nielsen, A. L., M. Oulad-Abdelghani, J. A. Ortiz, E. Remboutsika, P. Chambon, et al. 2001. Heterochromatin formation in mammalian cells: interaction between histones and HP1 proteins. *Mol. Cell.* 7:729–739.

15. Schmiedeberg, L., K. Weisshart, S. Diekmann, G. Meyer Zu Hoerste, and P. Hemmerich. 2004. High- and low-mobility populations of HP1 in heterochromatin of mammalian cells. *Mol. Biol. Cell.* 15:2819–2833.

16. Schotta, G., A. Ebert, V. Krauss, A. Fischer, J. Hoffmann, et al. 2002. Central role of *Drosophila* SU(VAR)3–9 in histone H3–K9 methylation and heterochromatic gene silencing. *EMBO J.* 21:1121–1131.

17. Cheutin, T., A. J. McNairn, T. Jenuwein, D. M. Gilbert, P. B. Singh, et al. 2003. Maintenance of stable heterochromatin domains by dynamic HP1 binding. *Science.* 299:721–725.

18. Festenstein, R., S. N. Pagakis, K. Hiragami, D. Lyon, A. Verreault, et al. 2003. Modulation of heterochromatin protein 1 dynamics in primary mammalian cells. *Science.* 299:719–721.

19. Krouwels, I. M., K. Wiesmeijer, T. E. Abraham, C. Molenaar, N. P. Verwoerd, et al. 2005. A glue for heterochromatin maintenance: stable SUV39H1 binding to heterochromatin is reinforced by the SET domain. *J. Cell Biol.* 170:537–549.

20. Dialynas, G. K., D. Makatsori, N. Kourmouli, P. A. Theodoropoulos, K. McLean, et al. 2006. Methylation-independent binding to histone H3 and cell cycle-dependent incorporation of HP1$\beta$ into heterochromatin. *J. Biol. Chem.* 281:14350–14360.

21. Cheutin, T., S. A. Gorski, K. M. May, P. B. Singh, and T. Misteli. 2004. In vivo dynamics of Swi6 in yeast: evidence for a stochastic model of heterochromatin. *Mol. Cell. Biol.* 24:3157–3167.

22. Wachsmuth, M., M. Caudron-Herger, and K. Rippe. 2008. Genome organization: balancing stability and plasticity. *Biochim. Biophys. Acta.* 1783:2061–2079.

23. Peters, A. H., D. O'Carroll, H. Scherthan, K. Mechtler, S. Sauer, et al. 2001. Loss of the Suv39h histone methyltransferases impairs mammalian heterochromatin and genome stability. *Cell.* 107:323–337.

24. Wachsmuth, M., and K. Weisshardt. 2007. Fluorescence photobleaching and fluorescence correlation spectroscopy: two complementary technologies to study molecular dynamics in living cells. *In* Imaging Cellular and Molecular Biological Functions. S. L. Shorte and F. Frischknecht, editors. Springer Verlag, Berlin/Heidelberg. 183–234.

25. Sprague, B. L., R. L. Pego, D. A. Stavreva, and J. G. McNally. 2004. Analysis of binding reactions by fluorescence recovery after photobleaching. *Biophys. J.* 86:3473–3495.

26. Wachsmuth, M., T. Weidemann, G. Muller, U. W. Hoffmann-Rohrer, T. A. Knoch, et al. 2003. Analyzing intracellular binding and diffusion with continuous fluorescence photobleaching. *Biophys. J.* 84:3353–3363.

27. Rabut, G., and J. Ellenberg. 2005. Photobleaching techniques to study mobility and molecular dynamics of proteins in live cells: FRAP, iFRAP, and FLIP. *In* Live Cell Imaging—A Laboratory Manual. R. D. Goldman and D. L. Spector, editors. Cold Spring Harbor Laboratory Press, Cold Spring Harbor, New York. 101–126.

28. Mueller, F., P. Wach, and J. G. McNally. 2008. Evidence for a common mode of transcription factor interaction with chromatin as revealed by improved quantitative fluorescence recovery after photobleaching. *Biophys. J.* 94:3323–3339.

29. Beaudouin, J., F. Mora-Bermúdez, T. Klee, N. Daigle, and J. Ellenberg. 2006. Dissecting the contribution of diffusion and interactions to the mobility of nuclear proteins. *Biophys. J.* 90:1878–1894.

30. Yamamoto, K., and M. Sonoda. 2003. Self-interaction of heterochromatin protein 1 is required for direct binding to histone methyltransferase, SUV39H1. *Biochem. Biophys. Res. Commun.* 301:287–292.

31. Eskeland, R., A. Eberharter, and A. Imhof. 2007. HP1 binding to chromatin methylated at H3K9 is enhanced by auxiliary factors. *Mol. Cell. Biol.* 27:453–465.

32. Zhang, K., K. Mosch, W. Fischle, and S. I. Grewal. 2008. Roles of the Clr4 methyltransferase complex in nucleation, spreading and maintenance of heterochromatin. *Nat. Struct. Mol. Biol.* 15:381–388.

33. Lu, B. Y., P. C. Emtage, B. J. Duyf, A. J. Hilliker, and J. C. Eissenberg. 2000. Heterochromatin protein 1 is required for the normal expression of two heterochromatin genes in *Drosophila*. *Genetics.* 155:699–708.

34. Stehr, R., N. Kepper, K. Rippe, and G. Wedemann. 2008. The effect of internucleosomal interaction on folding of the chromatin fiber. *Biophys. J.* 95:3677–3691.

Biophysical Journal, Volume 97

**Supporting Material**

# Multi-scale analysis of dynamics and interactions of heterochromatin protein 1 by fluorescence fluctuation microscopy

Katharina P. Müller, Fabian Erdel, Maïwen Caudron-Herger, Caroline Marth, Barna D. Fodor, Mario Richter, Manuela Scaranaro, Joël Beaudouin, Malte Wachsmuth, and Karsten Rippe

# Supplementary Methods

## Plasmids

Suv39h1 and HP1β cDNA fragments were derived by PCR from plasmids pGeX2T-Suv39h1 and pET-16b-HP1β, kindly provided by Ken Yamamoto (Kyushu University, Japan) and Natasha Murzina (University of Cambridge, UK). These were cloned into the vectors pEGFP-C1 (BD Biosciences Clontech, Heidelberg, Germany) or pTagRFP-C (Evrogen, Moscow, Russia), respectively, to generate expression vectors for the autofluorescent fusion proteins GFP-Suv39h1, TagRFP-Suv39h1, GFP-HP1β and TagRFP-HP1β. Labeling of chromatin was accomplished via mRFP1-labeled histone H2A by transient transfection (1).

## Cell lines

The stable GFP-HP1α cell line clone was isolated in a screen to identify mouse pericentric chromatin proteins. A retrovirus-based gene trap vector (pRet_1L-Neo, unpublished data) was used to infect NIH 3T3 cells. The vector carried a mouse PGK promoter-driven FLAG-HA-GFP cassette without a stop codon, followed by a splice donor site. The infected cells were screened for focal GFP enrichment, and the fusion partner was determined by 3'-race with GFP-specific primers. The sequence information obtained from the GFP-HP1α clone indicates that the GFP cassette is spliced to exon 7 of endogenous HP1α transcripts. In the predicted fusion protein product (FLAG-HA-eGFP-full-length-HP1α) an additional NLVAILLQVDQQAHD amino acid sequence (translation of the noncoding 5' region of exon 7) separates the two moieties. This cell line is referred to here as 3T3-HP1α. To investigate the contribution of the Suv39h1/h2 methylases on HP1 binding immortalized mouse embryonic fibroblast (iMEF) cells were used (2). In these experiments wild type (iMEF-wt) and double null mutant (iMEF-dn) cells were compared, in which the Suv39h1 and Suv39h2 gene loci were disrupted. Accordingly, the iMEF-dn cells lack H3K9 di- and trimethylation in pericentric heterochromatin.

## Cell culture

NIH 3T3 mouse fibroblasts, the 3T3-HP1α cell line as well as the iMEF-wt and the iMEF-dn cell lines were cultured in tissue culture flasks at 37 °C in a water-saturated 5 % $CO_2$ atmosphere, using Dulbecco modified eagle medium (DMEM) without phenol red, supplemented with 10 % fetal calf serum, 2 mM L-glutamine, penicillin/streptomycin (each at 100 µg/ml) and 0.35 g/ml glucose. For live imaging experiments cells were cultured to 60 – 80 % confluency on chambered microscopy slides (Nunc, Wiesbaden, Germany) as previously described and were kept in Leibovitz's L15-medium (Invitrogen, Karlsruhe, Germany) supplemented with 10 % fetal calf serum and pen/strep during live experiments. The measurements were carried out at room temperature. Transient transfection was performed with Effectene (Qiagen, Hilden, Germany) for NIH 3T3 cells and TurboFect (Fermentas, St. Leon-Roth, Germany) for iMEFs according to the protocol of the manufacturer. For imaging of fixed samples, the cells were incubated for 1 - 2 days after transfection and then fixed in 4 % paraformaldehyde (PFA) for 7 minutes at room temperature. Immunostaining of fixed cells was conducted with a primary anti-H3K9me3 antibody (Abcam, Cambridge, UK) and subsequent visualization with a secondary goat anti-rabbit Alexa 568 antibody (Invitrogen, Molecular Probes). Chromatin staining was accomplished with 5 µg/ml Hoechst 33342 or 0.5 µg/ml DAPI (Invitrogen, Molecular

Probes). All coverslips were mounted using Mowiol (10 % Mowiol 4-88, 25 % glycerol in 100 mM Tris·HCl pH 8.5).

## Western blot

NIH 3T3 cells stably expressing GFP-HP1α were harvested by trypsination and lysed in ice-cooled buffer containing 10 mM Tris·HCl pH 7.5, 150 mM NaCl, 0.5 mM EDTA, 0.1 % NP40, 1 mM PMSF, and a protease inhibitor cocktail (Roche, Mannheim, Germany). After SDS-PAGE the proteins were transferred to a nitrocellulose membrane (Whatman GmbH, Dassel, Germany) and incubated with the primary antibody anti-HP1α (1:1000 dilution, C7F11, Cell Signaling, Danvers, MA, USA) overnight at 4 °C, washed three times with TBS/0.1 % Tween and incubated with a secondary HRP-conjugated antibody (anti-rabbit, 1:2000 dilution, Cell Signaling, Danvers, MA, USA) for 1 hour and washed 3 times with TBS/0.1 % Tween. Bound antibodies were detected using a chemiluminescent ECL reagent (1 ml 0.1 M Tris·HCl pH 7.5 supplemented with 0.25 mg Luminol, 0.3 µl $H_2O_2$, 100 µl DMSO, 0.11 mg para-hydroxycumarine acid) and an imaging film. For quantification, DyLight 800-conjugated secondary antibodies (anti-rabbit, Pierce Biotechnology, Rockford, IL, USA) were used and the signal was recorded with a LI-COR Odyssey infrared detection system (LI-COR Biosciences, Bad Homburg, Germany).

## Fluorescence microscopy setup

For confocal imaging, FRAP and FLIP a Leica TCS SP5 confocal laser scanning microscope (CLSM) equipped with a HCX PL APO lambda blue 63x/1.4 NA oil immersion objective lens was used (Leica Microsystems CMS GmbH, Mannheim, Germany). A diode-pumped solid state laser and an Argon ion laser were used for DAPI ($\lambda = 405$ nm), GFP ($\lambda = 488$ nm) and TagRFP ($\lambda = 514$ nm) excitation. For the multi-color analysis sequential image acquisition was applied and emission detection ranges were adjusted to minimize crosstalk between the different signals. Protein distribution and chromatin density in heterochromatin respective to euchromatin were compared by evaluating multiple spots within a cell and calculating the mean intensity values therein.
FCS and CP measurements were performed on a Leica TCS SP2 AOBS FCS2 CLSM equipped with single photon counting modules for single molecule detection (SPC-AQR-14, Perkin Elmer Optoelectronics, Fremont, CA, USA). For intracellular measurements a HCX UPlanApo 63x/1.2 NA water immersion objective lens with correction collar was used. The excitation of GFP and Alexa Fluor 488 was done with the 488 nm Argon laser line. The detection pinhole had a diameter corresponding to one Airy disk and emission was recorded through a 500 - 550 nm filter. For FCS and CP measurements the scanning mirrors were fixed at a desired recording position and the fluorescence signal was acquired with the software Vista 3.6.22 LE (ISS Inc., Champaign, IL, USA).

## Fluorescence photobleaching experiments

For the FRAP experiments 50 prebleach images were taken. Laser intensities were adjusted such that the power in the sample did not exceed 10 µW, resulting in an energy deposition of less than 1 µJ per image for the selected scan speed (1400 Hz) and image size (128 x 128 pixels). The region of interest (ROI) was subjected to two high intensity laser pulses of 112 ms duration each corresponding to about two times an energy deposition of not more than 100 µJ. Postbleach images were collected at 112 ms time intervals for 60-100 s with the

laser intensity attenuated to the same as in the prebleach images. To characterize the slow mobility fraction in heterochromatin the data acquisition was extended to ~ 300 s. For the FRAP profile analysis a bar of 3 µm in height crossing the whole cell nucleus was photobleached, while the intensity-based analysis was conducted for a circular ROI of effective 1.9 µm in diameter. The illumination of the cells with relatively high laser intensity during the bleaching process could potentially compromise the integrity of the GFP tagged protein and change its mobility and interaction properties. Under the conditions used here the illumination during bleaching appears to have no significant effect since the analysis of HP1α mobility by methods with very different energy deposition (FRAP, CP and FCS, see below) gave consistent results. This is consistent with the previously reported findings that local heating during photobleaching does not exceed 0.5 K under the conditions used here and has no significant effect on macromolecular mobility (3-5). Furthermore, it was confirmed that multiple FRAP experiments in the same cell gave identical results within the error of the measurements. The cell viability was not affected, which is attributed to the fact that for fluorescent proteins the generation of free radicals is largely reduced as compared to synthetic dyes (6).

## Profile FRAP analysis (pFRAP)

An analysis of the bleach profile shape during the fluorescence recovery time course was conducted (7). The fluorescence intensity was averaged in parallel to the bleach strip to calculate the intensity profile perpendicular to the strip for each picture of the time series. The profiles were normalized to the averaged prebleach values and analyzed in terms of the profile broadening. For one-dimensional strip-bleaching the postbleach distribution as initial condition is given by

$$c(y_0,0) = 1 - p\big(\Theta(y_0 - a) - \Theta(y_0 + a)\big) \qquad (1)$$

with $\Theta$ being the unit step function, $a$ the half band width and $p$ corresponding to the bleach depth ($p = 0$ for non-bleached regions and $p = 1$ for a completely bleached ROI). The distribution for successive time-steps can then be calculated with Eq. 2:

$$c(y,t) = 1 - \frac{p}{2}\left[erf\left(\frac{a-y}{\sigma(t)}\right) + erf\left(\frac{a+y}{\sigma(t)}\right)\right] \qquad (2)$$

by applying the transition probability (Greens function) with the boundary condition of $\sigma = 0$ at $t = 0$. Since the dimensions of the bleached strip were of similar dimensions as the cell nucleus a confined diffusion model was applied. The value of $\sigma^2(t)$, corresponding to the mean squared displacement, was calculated according to $\sigma^2(t) = r_c^2\left(1 - \exp\left(-4Dt/r_c^2\right)\right)$ with $D$ being the diffusion coefficient and $r_c$ the typical length scale of the accessible region. The profiles of the first 50 postbleach images (according to 5.6 s) were plotted and the data were fitted to Eq. 2 using Microcal Origin 6.0 (OriginLab, Northampton, MA, USA).

## Intensity based FRAP experiments

Before fitting the data the FRAP recovery curves were corrected for acquisition photobleaching and detector noise. Image areas representing the cell and the background were selected, and the average intensity in both areas was calculated over time. For the

analysis the bleached circular region of interest (ROI) was selected and the normalized recovery curve – averaged over the selected ROI – was calculated according to the formula

$$frap(t) = \left(\frac{I_{\mathrm{ROI}}(t) - I_{\mathrm{BG}}(t)}{I_{\mathrm{Cell}}(t) - I_{\mathrm{BG}}(t)}\right)\left(\frac{I_{\mathrm{Cell}}(0) - I_{\mathrm{BG}}(0)}{I_{\mathrm{ROI}}(0) - I_{\mathrm{BG}}(0)}\right) \qquad (3)$$

with the average ROI intensity $I_{\mathrm{ROI}}(t)$, the average background intensity $I_{\mathrm{BG}}(t)$ and the average cell intensity $I_{\mathrm{Cell}}(t)$.

The time evolution of the intensity integrated over the bleach spot was analyzed according to the theoretical framework developed by McNally and coworkers (8). The size of the bleach spot (ROI) was approximated by a circle with an effective radius that accounts for the broadened initial bleach profile (9). It was determined from the intensity profile through the bleach spot measured for a fixed sample. From this a diameter of 1.5 µm corresponding to the microscope setting was measured at the bottom of the intensity profile, while the effective diameter at 50 % intensity was ~1.9 µm. The latter value was used for the quantitative analysis, in which the data were fitted either to a diffusion model, a binding model or a reaction-diffusion model that incorporates both diffusion and binding processes.

The recovery of the fluorescence intensity integrated over the bleach spot was analyzed according to the following approach: The FRAP recovery curve for the whole ROI equals the sum of the contributions from free $f$ or bound $c$ labeled protein $frap(t) = \bar{f}(t) + \bar{c}(t)$, with the horizontal bar indicating averages over the bleached ROI. In order to obtain a numerical solution a Laplace transform is performed and a solution for $\overline{frap}(p)$ is derived, which must be transformed back to give $frap(t)$. The parameter $p$ denotes the complex Laplace variable (8).

$$\overline{frap}(p) = \frac{1}{p} - \frac{F_{\mathrm{eq}}}{p}\left(1 - 2K_1(q\omega)I_1(q\omega)\right)\left(1 + \frac{k^*_{\mathrm{on}}}{p + k_{\mathrm{off}}}\right) - \frac{C_{\mathrm{eq}}}{p + k_{\mathrm{off}}} \qquad (4)$$

The parameters $k_{\mathrm{on}}$ and $k_{\mathrm{off}}$ and $[S]_{\mathrm{eq}}$ denote the association rate and the dissociation rate, and the relation $k^*_{\mathrm{on}} = k_{\mathrm{on}} \cdot [S]_{\mathrm{eq}}$ defines a pseudo-association rate $k^*_{\mathrm{on}}$ for the case of a constant equilibrium substrate concentration $[S]_{\mathrm{eq}}$. These are related to steady-state concentrations of free and bound protein $f_{\mathrm{eq}}$ and $c_{\mathrm{eq}}$, respectively, by

$$f_{\mathrm{eq}} = \frac{k_{\mathrm{off}}}{k^*_{\mathrm{on}} + k_{\mathrm{off}}}$$
$$c_{\mathrm{eq}} = \frac{k^*_{\mathrm{on}}}{k^*_{\mathrm{on}} + k_{\mathrm{off}}} \qquad (5)$$

$I_1$ and $K_1$ are modified Bessel functions of the first and second kind; $\omega$ is the radius of the bleach spot and $q^2$ is defined as

$$q^2 = \left(\frac{p}{D}\right)\left(1 + \frac{k^*_{\mathrm{on}}}{p + k_{\mathrm{off}}}\right) \qquad (6)$$

The numerical inverse Laplace transformation yields $frap$(t) that can be fitted to the recovery curve in order to obtain values for the fit parameters $k^*_{\mathrm{on}}$, $k_{\mathrm{off}}$ and the diffusion coefficient $D$. Based on the ratio of the rate constants derived from quantitative FRAP analysis, a pseudo-binding constant $K^*_{\mathrm{eq}}$ can be calculated according to Eq. 7:

$$K_{\mathrm{eq}}^{*} = \frac{k_{\mathrm{on}}^{*}}{k_{\mathrm{off}}} = \frac{k_{\mathrm{on}}^{*}[S]_{\mathrm{eq}}}{k_{\mathrm{off}}} \qquad (7)$$

Using the definition of the pseudo-binding constant, an apparent diffusion coefficient $D_{\mathrm{app}}$ is defined as

$$D_{\mathrm{app}} = \frac{D}{1 + K_{\mathrm{eq}}^{*}} \qquad (8)$$

This is the relevant quantity for the description of effective diffusion processes with $k_{\mathrm{on}}^{*}\tau_{\mathrm{D}} >> 1$, and a characteristic diffusion time $\tau_{\mathrm{D}} = \omega^{2}/D$ (8). In the case of multiple binding sites, Eq. 8 has to be modified to

$$D_{app} = \frac{D}{1 + \sum_{i} \theta_{\mathrm{i}} \cdot K_{\mathrm{eq,i}}^{*}} \qquad (9)$$

with the parameters $\theta_i$ representing the relative fractions of the different binding sites. The simpler diffusion-dominant and reaction-dominant models can be derived from the reaction-diffusion model (Eqs. 4-6), for which the appropriate simplifications and the inverse Laplace transform can be calculated analytically. For the diffusion-dominant case, the solution is

$$frap(t) = e^{-\frac{\tau_{\mathrm{D}}}{2t}}\left[I_0\left(\frac{\tau_{\mathrm{D}}}{2t}\right) + I_1\left(\frac{\tau_{\mathrm{D}}}{2t}\right)\right] \qquad (10)$$

and for the reaction-dominant case, the solution it is given by

$$frap(t) = 1 - C_{\mathrm{eq}}\, e^{-k_{\mathrm{off}} t} \qquad (11)$$

At least 10 experiments each for HP1α and for HP1β were evaluated for a specific type of bleaching experiment.

## Implementation of software for the analysis of FRAP recovery curves according to different models

*Reaction diffusion analysis*. For the half-automated FRAP analysis a software tool was implemented that is termed **F**RAP **RE**action **DI**ffusion **S**olver (*FREDIS*). *FREDIS* directly reads Leica Image Files (LIF) together with its metadata (such as the scanning speed, the acquisition time and the voxel size) that are generated by the Leica Application Suite software installed with the Leica TCS SP5 microscopes. The FRAP curve can be calculated and fitted to the models described by Eqs. 4, 10 and 11 for the determination of reaction-diffusion parameters according to the approach described previously (8). The reaction model assumes binding that is much slower than diffusion so that the latter can be neglected. The pure diffusion model describes freely diffusing proteins or transient binding with very fast exchange that is indistinguishable from a diffusive process. In contrast the reaction-diffusion model incorporates diffusion and binding effects on arbitrary time-scales. The fitting algorithm is based on a simple iterative grid search that minimizes the residuals

$$\chi^2 = \sum_i \frac{(frap_i - model_i)^2}{model_i} \qquad (12)$$

In Eq. 12 $frap_i$ represents the measured recovery at time-point $i$, $model_i$ represents the calculated recovery at time-point $i$ (the sum runs over all post-bleach time-points). The calculated recovery curve is fixed at the two points indicated by the red dots in the plot below: At time 0 after the bleach it was set to 0, since control experiments with fixed cells showed that the intensity was 0 after the bleach in all planes. At the time-point of the last acquired image it was set to the average ROI intensity of the last five images. In the case of incomplete recovery the size of the immobile fraction was estimated by calculating the value of the recovery curve at infinite time, and subtracting this value from the pre-bleach intensity (i.e. the average ROI intensity of the last five pre-bleach images).

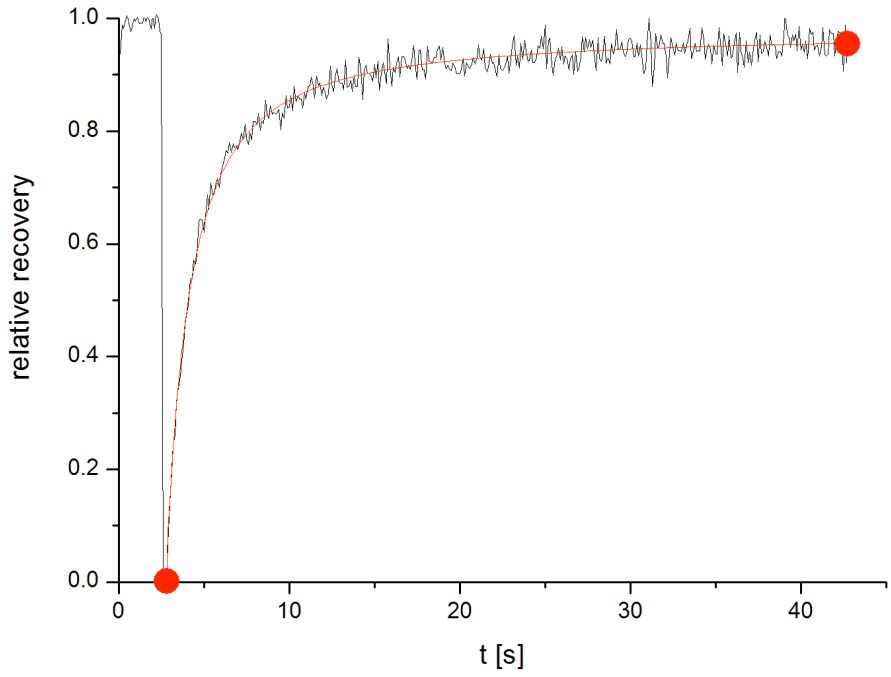


For the pure reaction and the pure diffusion model, the fitting procedure takes less than one second on a standard computer system. Thus, there is no demand for a faster second-order algorithm, and the robust grid search technique with an automatically generated initial guess can be used. However, the calculation of the recovery time course according to the reaction-diffusion model is computed numerically, and – due to the relatively slow numerical inversion of the Laplace transform – computation time is an issue. Since second-order algorithms for the reaction-diffusion model involve four inverse numerical Laplace transforms in each cycle (to calculate the gradient in three-dimensional parameter space), they are slower than the simple grid search algorithm: In comparison to the second-order Levenberg-Marquardt algorithm, the grid search algorithm converged with more cycles but needed less computational time for a typical fit. Therefore the grid search algorithm was implemented as the standard fitting procedure for all the three models.

*Confidence intervals*. The error limits in *FREDIS* are calculated for each fit parameter as 95 % confidence intervals. The limits of each interval are determined according to the log-likelihood criterion (10)

$$n\left[\log(\chi^2(\theta_0)) - \log(\chi^2(\theta))\right] \le \chi_p^2(\alpha) \qquad (13)$$

$\chi^2(\theta)$ represents the sum of residuals for a given parameter vector $\theta$, $\theta_0$ is the parameter vector in the minimum, $n$ is the number of data points (i.e. post-bleach time points), $\chi_p^2(\alpha)$ is the upper $\alpha$ percentage point for the $\chi^2$ distribution and $p$ is the number of fit parameters. Starting at the minimum, the fit parameters are varied in both directions according to a grid search algorithm until the condition given in Eq. 13 does not hold anymore. For the pure reaction and pure diffusion models, only one parameter has to be varied and the calculation is straightforward. However, for the reaction-diffusion model three parameters have to be varied and the shape of the confidence region has to be incorporated into the calculation. This is due to the fact that an increase in the residuals caused by the change of one fit parameter can be compensated by the change of another fit parameter. In order to obtain the correct confidence interval the parameters cannot be regarded as independent. The shape of the confidence region can be estimated considering the formulas for the reaction-diffusion model and its limiting cases, the effective diffusion model and the reaction model. For moderate pseudo-association rates and small or moderate dissociation rates (compared to the characteristic diffusion times), all of the three fit parameters influence the recovery significantly. In this case, the three parameters can be regarded as independent and the confidence region resembles a sphere. For large pseudo-association rates, the dynamic behavior can be described adequately by an effective diffusion coefficient that depends only on the ratio of pseudo-association and dissociation rate (8). This results in an increasingly deformed confidence region that resembles an ellipsoid. The two-dimensional projections of this ellipsoid is depicted below in the schematic representation of confidence regions and intervals for the reaction-diffusion model at the transition to the effective diffusion regime (panel A, B) and to the pure reaction regime (panel C, D).

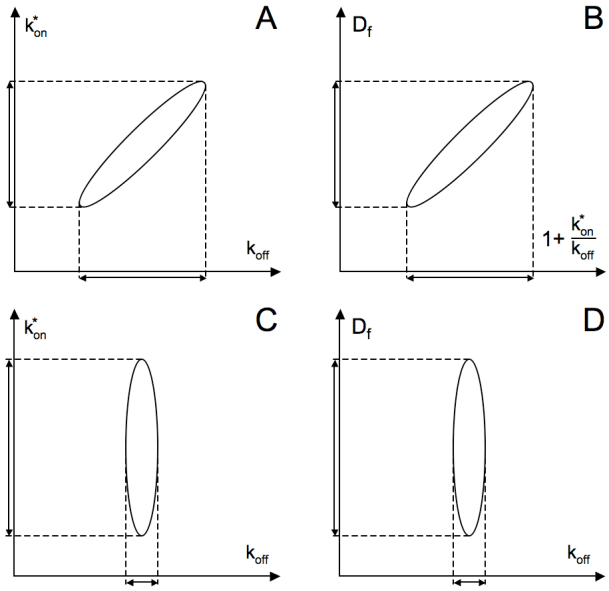


In the $k^*_{on} - k_{off}$ plane, i.e. at a fixed diffusion coefficient $D$, the projection of the confidence region is an ellipse: The effective diffusion coefficient depends only on the ratio of the rates that is constant on the semi-major axis of the ellipse. In the $D - k^*_{on}$ plane, the situation is similar: Since the effective diffusion coefficient can be kept constant by increasing (or

decreasing) both $D$ and $k_{on}^{*}$, the projection of the confidence region is elongated and resembles an ellipse (for sufficiently large $k_{on}^{*}$). In analogy, in the $D - k_{off}$ plane the effective diffusion coefficient can be kept constant by increasing $D$ and decreasing $k_{off}$ or vice versa, resulting in an elongated projection of the confidence region as well. For small pseudo-association rates (compared to the characteristic diffusion times), the pure reaction model can describe the dynamic behavior well: In this case, the recovery depends only on the dissociation rate, resulting in growing confidence intervals for both diffusion coefficient and pseudo-association rate. The shape of the confidence region is an ellipsoid with its semi-minor axis determining the confidence interval for the dissociation rate; the two-dimensional projections are ellipses with its semi-minor axis parallel to the axis of $k_{off}$ (see figure above). The case of diffusion is similar to the case of reaction: Instead of the dissociation rate the diffusion coefficient becomes the only important and well-defined parameter. Thus, the shape of the confidence region can be regarded as an ellipsoid that, in the case of effective diffusion, is not aligned to the axes spanning the parameter space. In this case, the confidence intervals calculated independently for the different fit parameters are too small. *FREDIS* calculates the independent 95 % confidence intervals for each parameter in the first step. Subsequently, the confidence intervals for $k_{on}^{*}$ and $k_{off}$ are calculated while both parameters are changed in a way that the effective diffusion coefficient is kept constant; the same is done for the diffusion coefficient $D$ (i.e. $k_{off}$ is adjusted in a way that the effective diffusion coefficient is kept constant). After this procedure, two confidence intervals have been determined for each fit parameter, and the larger one is reported. The independent confidence intervals for the fit parameters, which are calculated in the first step, determine the error of their ratios and are used in order to calculate the confidence intervals for all quantities depending on these ratios, i.e. the effective diffusion coefficient, the pseudo-affinity and the sizes of the free and the bound fraction.

*Evaluation of fit quality and comparison of different models*. For comparison between different experiments, the fit evaluation must be independent of the number of data points (unlike the sum of residuals $\chi^2$). *FREDIS* calculates the coefficient of determination $R^2$, which fulfills these requirements.

$$R^2 = \frac{\sum_i \left( frap_i - \overline{frap} \right)^2}{\sum_i \left( frap_i - model_i \right)^2} \qquad (14)$$

The parameter $frap_i$ denotes the value of the measured recovery curve at time-point $i$, $\overline{frap}$ is the mean of $frap_i$ and $model_i$ the value of the fitted recovery curve. For $R^2 = 1$, the measured and the calculated recovery curve are identical; for $R^2 = 0$, a horizontal line (at the mean of the measured recovery curve) would result in an equally good fit as the fit obtained.
The coefficient $R^2$ can be used to compare fits of models with the same number of parameters, i.e. to compare different data sets fitted with the same model to each other or to compare a data set fitted with the pure reaction model to a data set fitted with the pure diffusion model. However, if a fit with the reaction-diffusion model has to be compared to one of the simpler models, the different numbers of fit parameters have to be considered, since a fit is expected to be better if more fit parameters can be adjusted. Moreover, the fit with one of the simpler models cannot be better than the fit with the reaction-diffusion model because the simpler models are limiting cases of the reaction-diffusion model and all possible recovery curves calculated with the simpler models can be obtained with the appropriate

parameter set according to the reaction-diffusion model as well. In order to incorporate the different numbers of fit parameters into the analysis, the ratio $F$ is calculated

$$F = \frac{\chi_1^2 - \chi_2^2}{\chi_2^2} \frac{df_2}{df_1 - df_2} = \frac{\chi_1^2 - \chi_2^2}{\chi_2^2} \frac{n - p_2}{p_2 - p_1} \qquad (15)$$

with the sum of residuals for the fit with the $i$-th model $\chi_i^2$, the degrees of freedom for the $i$-th model $df_i$, the number of fit parameters for the $i$-th model $p_i$ and the number of data points $n$. The value of $F$ represents the ratio between the relative change in the sum of residuals and the relative change in degrees of freedom for the two models. In the calculation performed by *FREDIS*, the simpler model corresponds to model 1 and the reaction-diffusion model corresponds to model 2. Thus, an $F$ ratio greater than 1 means that the sum of residuals has decreased more than expected (going from the simpler model to the reaction-diffusion model) and the reaction-diffusion model is the better description. If the $F$ ratio is smaller than 1, the opposite is the case and the simpler model is the better description. Based on the $F$ ratio, a $P$ value is determined according to Eq. 16.

$$P = 1 - cdf_f(F, m, n) \qquad (16)$$

The parameter $cdf_f$ represents the cumulative density function for $F$ as defined in Eq. 15, $m$ and $n$ are the degrees of freedom of the nominator and the denominator. The $P$ value tests the null hypothesis that both models fit equally well to the data. It can be interpreted as the probability to obtain a given $F$ ratio (i.e. a given difference in the sum of residuals) by chance. Thus, a low $P$ value indicates a significant difference between the models, a high $P$ value only a slight difference. For every reaction-diffusion fit, *FREDIS* reports the $F$ and $P$ by comparing the reaction-diffusion model to the one of the two simple models that provides the better fit.

To extract the lower boundary for the dissociation rate of class I binding sites, reaction-diffusion fits with fixed values for the dissociation rate were performed and compared to fits according to the effective diffusion model. The fixed value for $k_{off}$ was reduced until the reaction-diffusion model fitted significantly worse than the effective diffusion model (according to the criterion given in Eq. 13). This value was considered to be the lower boundary for the dissociation rate.

## Continuous fluorescence photobleaching and fluorescence loss in photobleaching

For the CP experiments the laser beam of the CLSM was parked at the position of interest, and the bleaching process at moderate constant intensity was followed over time by recording the fluorescence emission signal. The dynamic equilibrium of photobleaching, diffusion, and dissociation/association processes of fluorescently labeled molecules to an immobilized structure leads to a characteristic decay of fluorescence as previously described in (7, 11, 12). The biphasic behavior of CP curves depends both on the bleaching of an immobilized or transiently bound fraction and on bleaching of the whole pool of freely mobile molecules. Between both fractions a dynamic exchange can take place. The binding interaction was considered as an equilibrium between a freely diffusing molecule $F$ and an immobile receptor S according to $F + S \leftrightarrows FS$, with the dissociation rate $k_{off}$ and the association rate $k_{on}$.

$$c_{immo}(\vec{r}, 0) / c_{diff}(\vec{r}, 0) = c_B(\vec{r})\, k_{on} / k_{off} \qquad (17)$$

The concentrations $c_{\text{immo}}$ and $c_{\text{diff}}$ describe the distribution of unbleached bound and free ligands, respectively, and $c_{\text{B}}$ denotes the constant concentration of available binding sites within the equilibrium. The diffusive particles contribute to the fluorescence signal according to

$$F_{\text{diff}}(t) = F_{\text{diff}}(0) \cdot \exp\left(-\left(\alpha + k_{\text{on}}\, c_B\right)\frac{V_{\text{eff}}}{V}\, t\right) \qquad (18)$$

where $\alpha$ is the fluorophore-specific bleaching probability, $V_{\text{eff}}$ the effective focal volume and $V$ the sample volume. Especially the initial decay in the time course of the fluorescence signal is primarily influenced by photobleaching the permanently immobilized molecules ($k_{\text{off}} = 0$)

$$F_{\text{immo}}(t) = F_{\text{immo}}(0) \cdot \left(1 + \frac{\alpha t}{2} + \frac{\alpha^2 t^2}{6}\right)^{-1} \qquad (19)$$

as well as the (transiently) bound fractions. Transiently bound HP1 features small dissociation rates, thus the particular case of $k_{\text{off}}/\alpha \leq 1$ holds (12):

$$F_{\text{bound}}(t) = F_{\text{bound}}(0) \cdot \left[\begin{array}{l} \left(\left(1 + \frac{\alpha t}{2} + \frac{\alpha^2 t^2}{6}\right)^{-1} - \frac{12\, k_{\text{off}}/\alpha}{5 + 14\, k_{\text{off}}/\alpha}\left(1 + \frac{3\alpha t}{7}\right)^{-1}\right)\exp\left(k_{\text{off}}\, t\right) \\ + \frac{12\, k_{\text{off}}/\alpha}{5 + 14\, k_{\text{off}}/\alpha}\exp\left(-\left(\alpha + k_{\text{on}}\, c_B\right)\frac{V_{\text{eff}}}{V}\, t\right) \end{array}\right] \qquad (20)$$

Therefore the measured fluorescence signal was fitted to the sum of these terms $F_{\text{immo}}(t) + F_{\text{bound}}(t) + F_{\text{diff}}(t)$. Data fitting was performed using a Levenberg-Marquardt algorithm.

In FLIP experiments the fluorescence loss within heterochromatin and euchromatin regions was monitored at low laser power between repetitive bleach pulses (every 1.35 s, within a circular ROI of 3 µm in diameter at 100 % laser intensity) at distant regions from the bleach spot within the same nucleus. The acquisition of 10 prebleach images was followed by 200 postbleach-images. Data were corrected for background and acquisition photobleaching and were normalized (13). The relative fluorescence was plotted against time and the differences in fluorescence between heterochromatin and euchromatin were calculated.

## Fluorescence correlation spectroscopy

Confocal images were taken to determine the regions for the fluctuation measurements in cytoplasm, euchromatin and heterochromatin. Then the concentration fluctuations of fluorescently labeled molecules (around the mean intensity) $\delta F(t) = F(t) - \langle F(t)\rangle$ were recorded for 60 s and the intensity signal was subjected to a time correlation analysis to obtain the autocorrelation function (ACF)

$$G(\tau) = \frac{\langle \delta F(t)\, \delta F(t+\tau)\rangle}{\langle F(t)\rangle^2} \qquad (21)$$

as described previously (7, 14, 15). The data were fitted to an anomalous diffusion model, which is characterized by a nonlinear time dependency of the mean squared particle displacement given by the anomaly parameter $\alpha$ (7, 16-19):

$$\left\langle r^2(t)\right\rangle = 2n\,D(t)\,t \propto t^{\alpha} \qquad (22)$$

Additional parameters for fitting the FCS curve include the intrinsic photophysical dynamics of the fluorescent proteins, like triplet states, whose probability is given by $\theta$ and whose relaxation time is $\tau_T$ (20), yielding Eq. 23:

$$G(\tau) = \frac{1}{N}\left(1-\theta+\theta\exp\left(-\frac{\tau}{\tau_T}\right)\right)\cdot\left(1+\left(\frac{\tau}{\tau_{\text{diff}}}\right)^{\alpha}\right)^{-1}\left(1+\frac{1}{\kappa^2}\left(\frac{\tau}{\tau_{\text{diff}}}\right)^{\alpha}\right)^{-1/2} \qquad (23)$$

Here $N$ represents the number of particles and $\tau_{\text{diff}} = \omega_0^2/4D$ the mean dwell time inside the focus with a lateral radius $\omega_0$. The structure parameter $\kappa$ is the ratio of the axial and lateral focus radius. Correlation data were fitted either to a one- or two-component model of anomalous diffusion or to a two-component model, where the first component followed anomalous diffusion and the second component was assumed to be bound to a slowly, confinedly moving lattice. The simplest way to model confined diffusion due to binding is to regard Brownian motion within a harmonic potential (with the friction coefficient $\gamma$ and the spring constant $k$) (21). Therefore the second component of the ACF changes to:

$$\begin{aligned} G_{\text{bound}}(\tau) &= \frac{1}{N}\left(1-\theta+\theta\exp\left(-\frac{\tau}{\tau_T}\right)\right) \\ &\cdot\left[\left(1+\frac{1-\exp\left(-k\tau/\gamma\right)}{\eta}\right)^{-1}\left(1+\frac{1-\exp\left(-k\tau/\gamma\right)}{\kappa^2\eta}\right)^{-1/2} - \left(1+\frac{1}{\eta}\right)^{-1}\left(1+\frac{1}{\kappa^2\eta}\right)^{-1/2}\right] \end{aligned} \qquad (24)$$

$\eta$ is the ratio of $\tau_{\text{diff}}$, the dwell time of free diffusion within the focal volume, and the relaxation time $\tau_{\text{relax}} = \gamma/k$. The calculation of the correlation functions was done with the Fluctuation Analyzer software (version 1.1 by M. Wachsmuth). Curve fitting was done with a fixed triplet correction term of $\tau_T$ = 100 µs for GFP. From the *in vivo* measurements we obtained the number of molecules $N$ and a diffusion-induced correlation time $\tau_{\text{diff}}$. Based on $N$ and $\tau_{\text{diff}}$ the molecule concentration $c = N/V_{\text{eff}}$ and the apparent diffusion coefficients $D = \omega_0^2/4\tau_{\text{diff}}$ can be calculated.

The calibration of the focal volume dimensions was done with Alexa Fluor 488 C5 maleimide (Invitrogen, Molecular Probes) dissolved in water, which has a diffusion coefficient of $D_{\text{Alexa488}} = (2.1 \pm 0.21)\cdot 10^{-6}$ cm²/s (21). The diffusion coefficient of Alexa Fluor 488 in water was used to measure the device-specific parameter $\kappa$ and calculate the lateral and axial beam dimension ($\omega_0 = \sqrt{4D_{\text{Alexa}}\tau_{\text{Alexa}}}$ and $z_0 = \kappa\omega_0$) as well as the effective focus volume $V_{\text{eff}} = \pi^{3/2}\omega_0^2 z_0$. The averaged values of $\omega_0$ and $z_0$ were $0.17 \pm 0.01$ µm and $0.78 \pm 0.06$ µm and therefore the observation volume was about $0.13 \pm 0.01$ fl. At least 10 experiments each for HP1α and for HP1β in the three compartments cytoplasm, euchromatin and heterochromatin were evaluated.

## Comparing diffusion coefficients obtained by FCS and FRAP

The effective diffusion coefficient for class I binding determined in heterochromatin by FRAP was $D_{FRAP} = 0.9 \pm 0.5$ µm² s$^{-1}$, the corresponding value determined by FCS was $D_{FCS} = 3.9 \pm 0.9$ µm² s$^{-1}$. Since these were determined on different length scales, the diffusion constants were related according to Eq. 25:

$$\frac{D_{FCS}}{D_{FRAP}} = \left( \frac{{w_{FCS}}^2}{{w_{FRAP}}^2} \right)^{(\alpha-1)/\alpha} = \left( \frac{(170\ \text{nm})^2}{(950\ \text{nm})^2} \right)^{(\alpha-1)/\alpha} \qquad (25)$$

Based on the anomaly parameter $\alpha$ that was determined to be $0.81 \pm 0.04$ in euchromatin and $0.88 \pm 0.12$ in heterochromatin $D_{FCS}/D_{FRAP} = 2.2$ [1.8 … 2.8] in euchromatin and $D_{FCS}/D_{FRAP} = 1.6$ [1.0 … 3.0] in heterochromatin was calculated from Eq. 25.

## References


1. Jegou, T., I. Chung, G. Heuvelmann, M. Wachsmuth, S. M. Görisch, K. Greulich-Bode, P. Boukamp, P. Lichter, and K. Rippe. 2009. Dynamics of telomeres and promyelocytic leukemia nuclear bodies in a telomerase negative human cell line. Mol. Biol. Cell 20:2070-2082.
2. Peters, A. H., D. O'Carroll, H. Scherthan, K. Mechtler, S. Sauer, C. Schofer, K. Weipoltshammer, M. Pagani, M. Lachner, A. Kohlmaier, S. Opravil, M. Doyle, M. Sibilia, and T. Jenuwein. 2001. Loss of the Suv39h histone methyltransferases impairs mammalian heterochromatin and genome stability. Cell 107:323-337.
3. Axelrod, D. 1977. Cell surface heating during fluorescence photobleaching recovery experiments. Biophys J 18:129-131.
4. Simon, J. R., A. Gough, E. Urbanik, F. Wang, F. Lanni, B. R. Ware, and D. L. Taylor. 1988. Analysis of rhodamine and fluorescein-labeled F-actin diffusion in vitro by fluorescence photobleaching recovery. Biophys J 54:801-815.
5. Jain, R. K., R. J. Stock, S. R. Chary, and M. Rueter. 1990. Convection and diffusion measurements using fluorescence recovery after photobleaching and video image analysis: in vitro calibration and assessment. Microvasc Res 39:77-93.
6. Tour, O., R. M. Meijer, D. A. Zacharias, S. R. Adams, and R. Y. Tsien. 2003. Genetically targeted chromophore-assisted light inactivation. Nat Biotechnol 21:1505-1508.
7. Wachsmuth, M., and K. Weisshardt. 2007. Fluorescence Photobleaching and Fluorescence Correlation Spectroscopy: Two Contemplementary Technologies To Study Molecular Dynamics in Living Cells. In Imaging Cellular and Molecular Biological Functions. S. L. Shorte, and F. Frischknecht, editors. Springer Verlag, Berlin, Heidelberg. 183-234.
8. Sprague, B. L., R. L. Pego, D. A. Stavreva, and J. G. McNally. 2004. Analysis of binding reactions by fluorescence recovery after photobleaching. Biophys J 86:3473-3495.
9. Mueller, F., P. Wach, and J. G. McNally. 2008. Evidence for a common mode of transcription factor interaction with chromatin as revealed by improved quantitative fluorescence recovery after photobleaching. Biophys J 94:3323-3339.
10. Seber, G. A. F., and C. J. Wild. 2003. Nonlinear Regression. John Wiley and Sons, New York.
11. Wachsmuth, M., M. Caudron-Herger, and K. Rippe. 2008. Genome organization: Balancing stability and plasticity. Biochim Biophys Acta 1783:2061-2079.
12. Wachsmuth, M., T. Weidemann, G. Muller, U. W. Hoffmann-Rohrer, T. A. Knoch, W. Waldeck, and J. Langowski. 2003. Analyzing intracellular binding and diffusion with continuous fluorescence photobleaching. Biophys. J. 84:3353-3363.
13. Rabut, G., and J. Ellenberg. 2005. Photobleaching Techniques to Study Mobility and Molecular Dynamics of Proteins in Live Cells: FRAP, iFRAP, and FLIP. In Live Cell

Imaging - A laboratory manual. R. D. Goldman, and D.L.Spector, editors. Cold Spring Harbor Laboratory Press, Cold Spring Harbor, New York. 101-126.
14. Schwille, P. 2001. Fluorescence Correlation Spectroscopy and Its Potential for Intracellular Applications. Cell Biochemistry and Biophysics 34:383-408.
15. Haustein, E., and P. Schwille. 2003. Ultrasensitive investigations of biological systems by fluorescence correlation spectroscopy. Methods 29:153-166.
16. Saxton, M. J. 1994. Anomalous diffusion due to obstacles: a Monte Carlo study. Biophys. J. 66:394-401.
17. Schwille, P., J. Korlach, and W. W. Webb. 1999. Fluorescence correlation spectroscopy with single-molecule sensitivity on cell and model membranes. Cytometry 36:176-182.
18. Masuda, A., K. Ushida, and T. Okamoto. 2005. New fluorescence correlation spectroscopy enabling direct observation of spatiotemporal dependence of diffusion constants as an evidence of anomalous transport in extracellular matrices. Biophys J 88:3584-3591.
19. Wachsmuth, M., W. Waldeck, and J. Langowski. 2000. Anomalous diffusion of fluorescent probes inside living cell nuclei investigated by spatially-resolved fluorescence correlation spectroscopy. J Mol Biol 298:677-689.
20. Widengren, J., Ü. Mets, and R. Rigler. 1995. Fluorescence Correlation Spectroscopy of Triplet States in Solution: A Theoretical and Experimental Study. J. Phys. Chem. 99:13368-13379.
21. Wachsmuth, M. 2001. Fluoreszenzfluktuationsmikroskopie: Entwicklung eines Prototyps, Theorie und Messung der Beweglichkeit von Biomolekülen im Zellkern. In Fakultät für Physik und Astronomie. Ruprecht-Karls-Universität Heidelberg, Heidelberg.
22. Humphrey, W., A. Dalke, and K. Schulten. 1996. VMD: visual molecular dynamics. J Mol Graph 14:33-38, 27-38.
23. Ormo, M., A. B. Cubitt, K. Kallio, L. A. Gross, R. Y. Tsien, and S. J. Remington. 1996. Crystal structure of the Aequorea victoria green fluorescent protein [see comments]. Science 273:1392-1395.
24. Pearlman, D. A., D. A. Case, J. W. Caldwell, W. R. Ross, T. E. Cheatham III, S. DeBolt, D. Ferguson, G. Seibel, and P. Kollman. 1995. AMBER, a computer program for applying molecular mechanics, normal mode analysis, molecular dynamics and free energy calculations to elucidate the structures and energies of molecules. Comp. Phys. Commun. 91:1-41.
25. Case, D. A., T. A. Darden, T. E. I. Cheatham, C. L. Simmerling, J. Wang, R. E. Duke, R. Luo, K. M. Merz, D. A. Pearlman, M. Crowley, R. Walker, W. Zhang, B. Wang, S. Hayik, A. Roitberg, G. Seabra, K. F. Wong, F. Paesani, X. Wu, S. Brozell, V. Tsui, H. Gohlke, L. Yang, C. Tan, J. Mongan, V. Hornak, G. Cui, P. Beroza, D. H. Mathews, C. Schafmeister, W. S. Ross, and P. A. Kollman. 2006. Amber 9. University of California, San Francisco.
26. Garcia De La Torre, J., M. L. Huertas, and B. Carrasco. 2000. Calculation of hydrodynamic properties of globular proteins from their atomic-level structure. Biophys. J. 78:719-730.

## Supplementary Tables

### Table S1. Hydrodynamic calculations for HP1 and GFP-tagged HP1.

| | GFP | HP1 | $(HP1)_2$ | GFP-HP1 | GFP-HP1·HP1 | $(GFP-HP1)_2$ |
|---|---|---|---|---|---|---|
| $M$ (kDa) | 25.6 | 21.4 | 42.8 | 48.5 | 71.3 | 99.8 |
| $\bar{V}$ (kDa) | 0.736 | 0.726 | 0.726 | 0.729 | 0.73 | 0.73 |
| $f$ ($\mu m^2\ s^{-1}$) | $4.8 \cdot 10^{-11}$ | $6.1 \cdot 10^{-11}$ | $7.5 \cdot 10^{-11}$ | $6.6 \cdot 10^{-11}$ | $7.6 \cdot 10^{-11}$ | $8.5 \cdot 10^{-11}$ |
| $D_{H2O}$ ($\mu m^2\ s^{-1}$) | 103.0 | 76.1 | 61.2 | 69.8 | 61.4 | 54.6 |
| $D_{cell}$ ($\mu m^2\ s^{-1}$) | 33.1 | 24.4 | 19.6 | 22.3 | 19.6 | 17.5 |

From a model structure of HP1 the basic hydrodynamic properties were calculated and the diffusion coefficients of GFP, HP1, and HP1 constructs in water were derived. $M$ is the molecular weight, $\bar{v}$ is the partial specific volume, $f$ is the friction coefficient and $D$ is the diffusion coefficient at 25 °C. The value of $D_{cell}$ includes an apparent 3.5 times higher intracellular viscosity than that of pure water (as determined for GFP). The molecular visualization program VMD (visual molecular dynamics, www.ks.uiuc.edu/Research/vmd, (22)) was used to build structures of mouse HP1β dimers fused to GFP by employing the corresponding crystal structures (23). The 14 amino acid linker between HP1 and GFP was modeled as a random coil. The energy-minimizing procedure and short molecular dynamics simulations were carried out with Amber 9 (http://ambermd.org/, (24, 25)). Hydrodynamic parameters were calculated with the program HYDROPRO with a sphere radius of 3.1 Å (version 7c, 2005; (26)). Molecular weight and the partial specific volume $\bar{v}$ were calculated using the program Sednterp (Sedimentation interpretation program, version 1.09, Hayes D.B. et al, University of New Hampshire, 1995).

**Table S2. Concentrations of endogenous HP1α and GFP-HP1α in NIH 3T3 cells.**

| | Cytoplasm (µmol liter$^{-1}$) | Euchromatin (µmol liter$^{-1}$) | Heterochromatin [a] (µmol liter$^{-1}$) |
|---|---|---|---|
| GFP-HP1α [b] | 0.16 ± 0.11 | 0.87 ± 0.07 | 2.1 ± 0.3 |
| HP1α (one allele) [b] | 0.04 ± 0.03 | 0.21 ± 0.03 | 0.5 ± 0.1 |
| endogenous HP1α [c] | 0.08 ± 0.05 | 0.41 ± 0.05 | 1.0 ± 0.2 |

The concentration of GFP-HP1α was determined by FCS measurements as the number of particles within the effective focus volume. Thus, in the table the particle concentrations are listed and the total concentration of monomeric HP1α units will depend on its association state in the cell. In the cytoplasm the diffusion coefficients determined by FCS indicate the presence of HP1α monomers, while the higher concentrations in the nucleus could promote the dimerization of HP1α.

[a] The HP1 concentration in heterochromatin were corrected for the 10 % immobile fraction within heterochromatin, which was bleached during FCS measurements.

[b] Concentrations refer to the 3T3-HP1α cell line that stably expresses GFP-HP1α. Endogenous HP1α concentrations in this cell line were determined from the ratio of GFP-HP1α to HP1α measured on quantitative Western blots (Fig. S3 B) and represent the expression level of HP1α from one allele.

[c] HP1α concentrations were calculated for two alleles, corresponding to the HP1α concentration in NIH 3T3 reference cells.

## Supplementary Figures

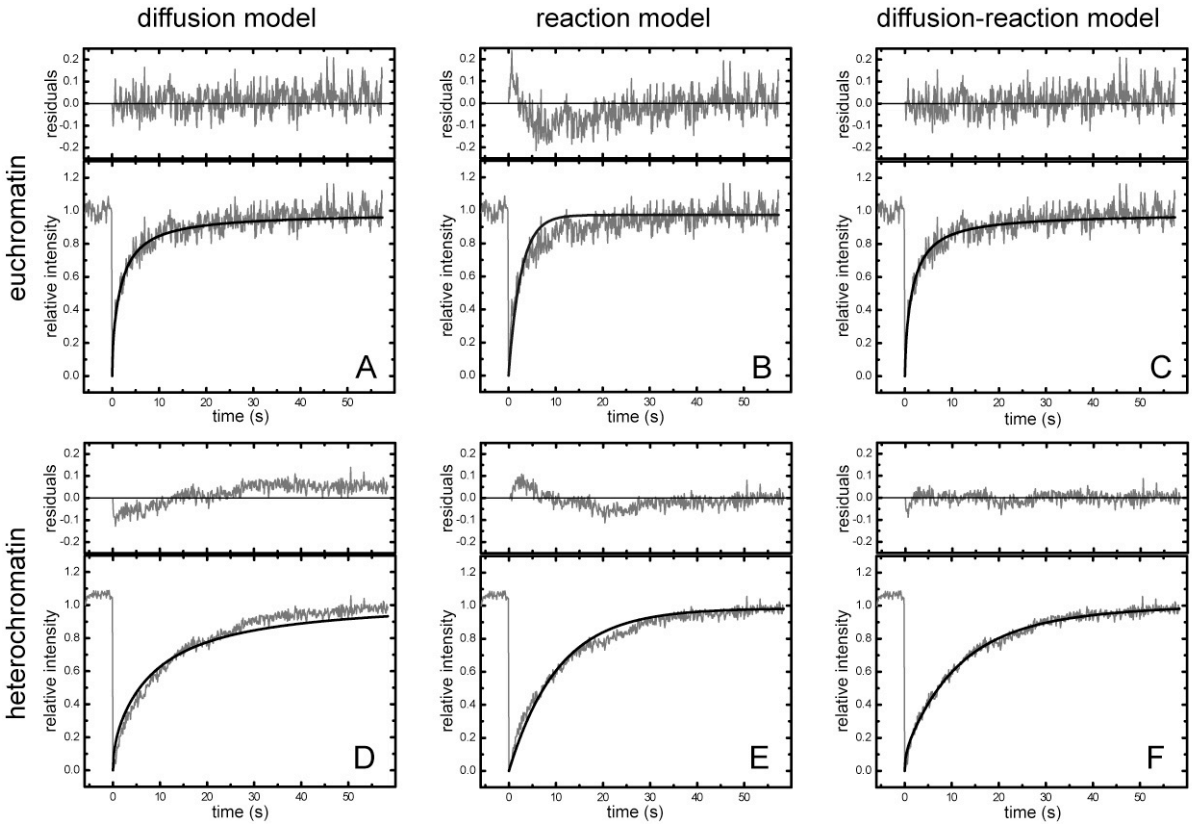


**Figure S1.** Kinetic modeling of the FRAP data recorded for HP1α in the 3T3-HP1α cell line in euchromatin (A-C) and heterochromatin (D-F). As described above three different mathematical models were used for curve fitting, a diffusion-dominant model (A, D; Eq. 10), a reaction-dominant model (B, E; Eq. 11) and a diffusion-reaction model that combines both reaction processes (C, F; Eq. 11). Above the graphs the residuals of the fits are shown. While for euchromatin a pure diffusion model resulted in a good fit, the description of HP1α mobility in heterochromatin required the use of the diffusion-reaction model for a good fit to the data. This was confirmed in a statistical test, in which an average value of $F = 94$ according to Eq. 15 was obtained in a comparison with the simpler models.

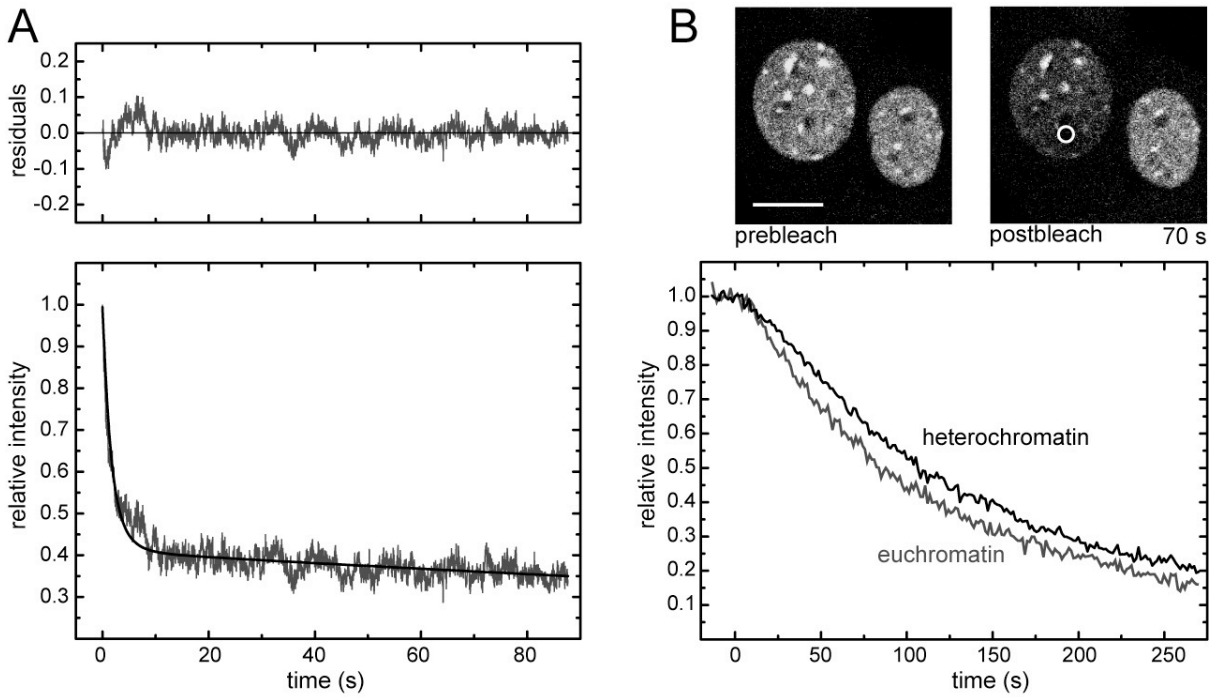


**Figure S2.** Continuous fluorescence photobleaching and fluorescence loss in photobleaching experiments. (**A**) The initial fast decay of the curve in the continuous photobleaching experiments corresponds to the bleaching of bound GFP-HP1 molecules. From the subsequent continuous exchange of molecules the kinetic dissociation rate $k_{off}$ is determined as described in the text. (**B**) Averaged FLIP curves of heterochromatin versus euchromatin loci within the same cell are depicted. The difference reveals the stably bound 10 % fraction of GFP-HP1α only present in heterochromatin.

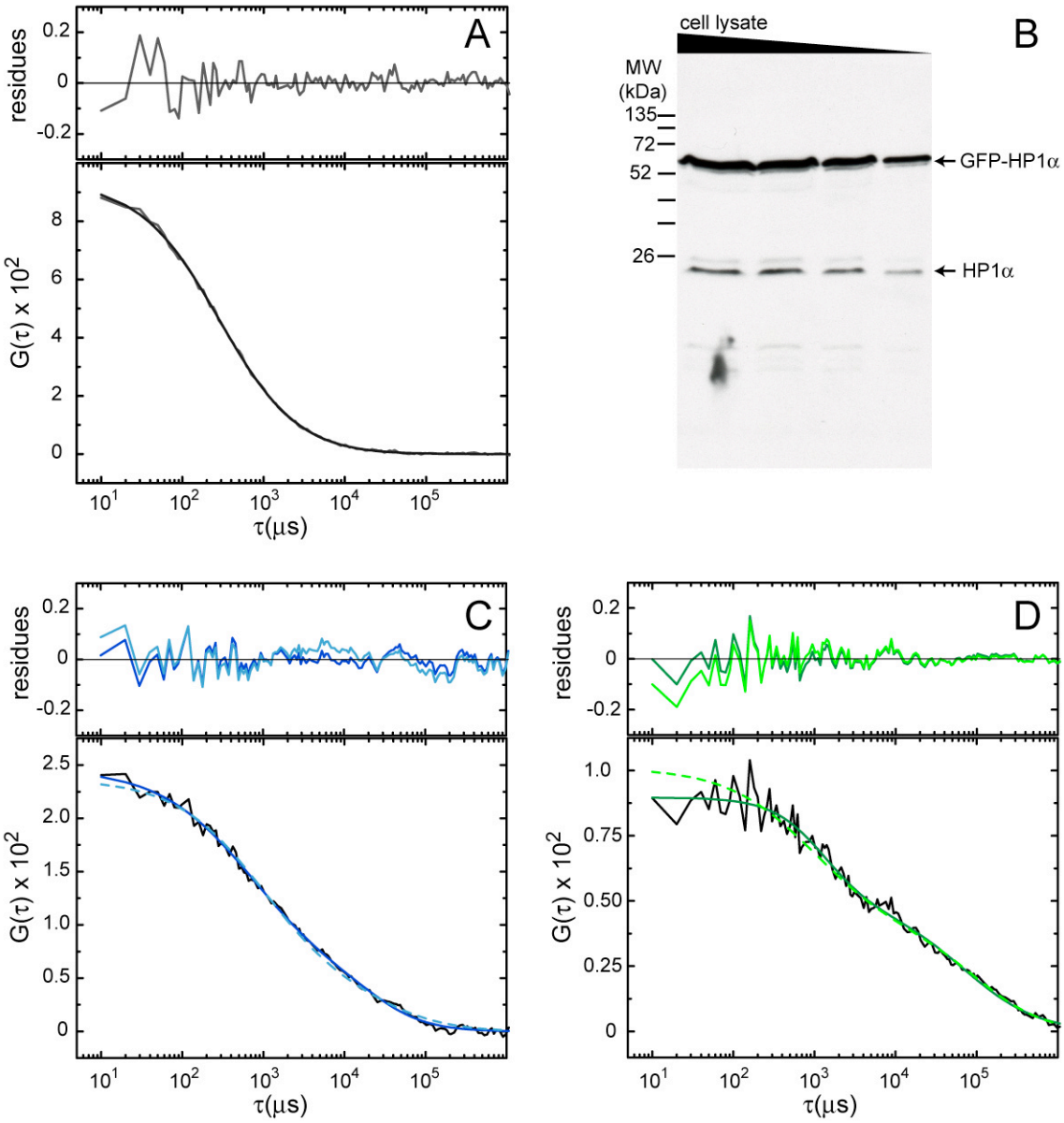


**Figure S3**. Analysis of HP1α in different cellular compartments by FCS. (**A**) ACF of HP1α in the cytoplasm fitted with an anomalous diffusion model. HP1α concentrations were determined by FCS experiments as the number of particles within the effective focus volume as described above and in Table S2. (**B**) The concentration of endogenous HP1α was determined from the ratio of GFP-tagged HP1α to untagged HP1α in the stable GFP-HP1α cell line by quantitative Western blots with an HP1α antibody. The two bands corresponding to GFP-HP1α and endogenous HP1α can be clearly identified. The concentration of endogenous HP1α can be determined by the relative ratio of the two signals on the western blot and the FCS concentration measurement of GFP-HP1α. (**C**) Representative ACF in euchromatin. The second fraction is likely to represent HP1α bound to slowly moving chromatin. Accordingly, the data were also fitted to a confined diffusion model (dashed curves), leading to an equally good fit as the anomalous diffusion description (solid line). (**D**) Same as in panel C but for heterochromatin.